Alma Mater Studiorum – Università di Bologna

DOTTORATO DI RICERCA IN

MECCANICA E SCIENZE AVANZATE DELL'INGEGNERIA (DIMSAI)

Ciclo XXXIV

Settore Concorsuale: 09/B1 – TECNOLOGIE E SISTEMI DI LAVORAZIONE

Settore Scientifico Disciplinare: ING-IND/16 – TECNOLOGIE E SISTEMI DI LAVORAZIONE

METAL ADDITIVE MANUFACTURING OF SOFT MAGNETIC MATERIAL FOR ELECTRIC MACHINES

Presentata da: Giuseppe Valli

Coordinatore Dottorato
Marco Carricato

Supervisore
Alessandro Fortunato

Co-supervisore
Lorenzo Donati

Esame finale anno 2022

Acknowledgements

My gratitude goes to the persons who helped me in Bologna on a daily basis as my supervisors Alessandro, Lorenzo, Alessandro, and Luca.

I would like to offer my special thanks to my family, particularly my mother Valentina, father Leonardo, sister Irene and his boyfriend Federico, for their unwavering love and support over the years. I'd like to express my gratitude for never making me feel lonely and for accepting me for who I am.

I'd also want to express my gratitude to all my close pals. I'm not sure how you manage to put up with my frequent disappearances. You have no idea how fortunate I am to have you in my life; you have taught me so much throughout the course of our relationship, and you have shaped me into the person I am today.

Finally, I am deeply grateful to my lovely partner Carlotta and her family. She is an incredibly intelligent, attractive, and kind lady whom I wish I had met sooner.

Thank you for your love and support.

Summary

LIST OF TABLES

LIST OF FIGURES

Abstract

This research work concerns the application of additive manufacturing (AM) technologies in new electric mobility sectors. The unmatched freedom that AM offers can potentially change the way electric motors are designed and manufactured. The thesis investigates the possibility of creating optimized electric machines that exploit AM technologies, with potential in various industrial sectors, including automotive and aerospace. In particular, we will evaluate how the design of electric motors can be improved by producing the rotor core using Laser Powder Bed Fusion (LPBF) and how the resulting design choices affect component performance. First, the metallurgical and soft magnetic properties of the pure iron and silicon iron alloy parts (Fe-3% wt.Si) produced by LPBF will be defined and discussed, considering the process parameters and the type of heat treatment. This research shows that using LPBF, both pure iron and iron silicon, the parts have mechanical and magnetic properties different from the laminated ones. Hence, FEM-based modeling will be employed to design the rotor core of an SYN RM machine to minimize torque ripple while maintaining structural integrity. Finally, we suggest that further research should extend the field of applicability to other electrical devices.

Chapter I. Introduction

A variety of industries have established electrical machines as critical components, both in terms of motors and generators, since the first half of the 19th century. Magnetic energy is converted into mechanical if used like motors, or mechanical torque is transformed into electromotive force if used in the form of generators. Emission standards for climate change increase the demand for vehicle electrification due to increasingly rigorous concerns.

Multiple disciplines, including materials, manufacturing, and design Figure 1 (Krings *et al.*, 2017), are growing interest in more efficient electric machines and is not surprising an increase in research efforts about this matter.

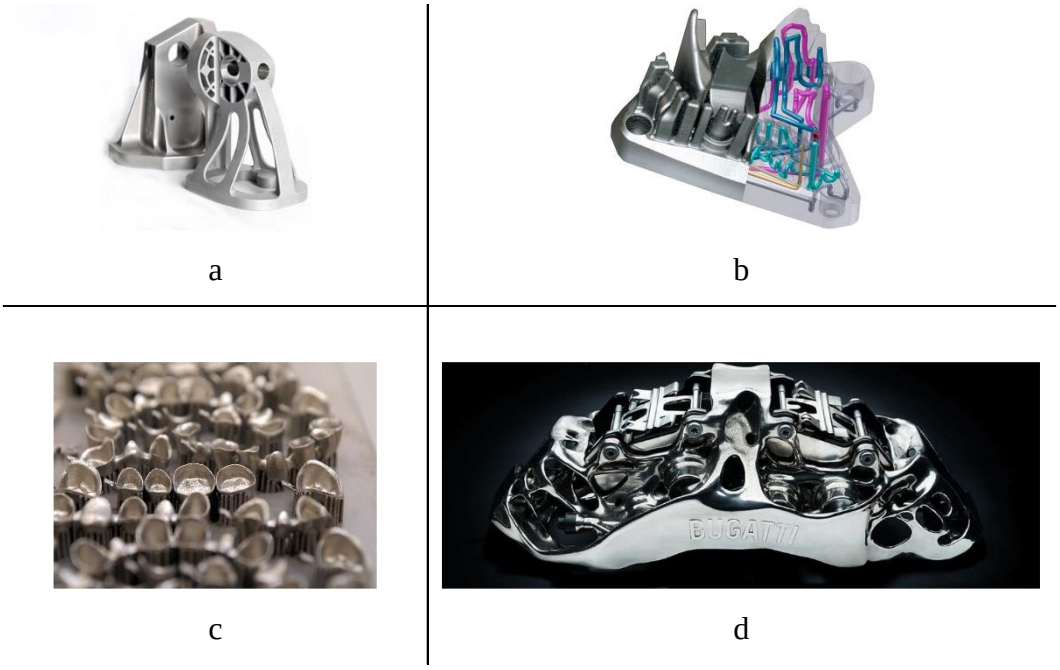

Figure 1 Examples of metal employment in a number of applications and industrial sectors. optimised bracket for an Airbus A380, with conventional bracket behind (a), tooling (b), dental implant by EOS (c) ugatti 3D-prints titanium brake calipers for its Chiron sports car.

Some examples of metal employment in a number of applications and industrial sectors are in Figure 1: an optimised bracket for an Airbus A380, with conventional bracket behind (a), tooling (b), dental implant by EOS (c) ugatti 3D-prints titanium brake calipers for its Chiron sports car ("Airbus - https://www.airbus.com," 2020; "Renishaw - https://www.renishaw.com," 2020; "EOS Gmbh - https://www.eos.info/en," 2020; "Bugatti - https://www.bugatti.com/," 2020).

A wide range of metallic materials, like steels, titanium, aluminum (Tonelli *et al.*, 2020) and their application using AM technologies were investigated. Processing of soft magnetic materials (SMM) by AM is limited to a few contributions in recent years (Garibaldi, Gerada and Hague, 2018), and a clear gap appears concerning the potential of LPBF on the development of electric motors in the automotive field.

The investigation of benefits for SMM in AM is the aim of this research, from a design to process perspective. The best choice to test AM potential would be through a completely new design without limitation. We started from an existing structure and modified it considering the magnetic properties of SMM produced by LPBF.

This research for re-design for AM is based on the literature review and criteria above; a rotor core of the synchronous machine is selected to be optimized and will be chosen an SMM compatible with LPBF process, pure iron, or silicon iron. Microstructural and mechanical properties of the SMM will be evaluated; the re-design process will consider the material properties of additively manufactured materials to grant the best torque ripple of the electrical machine.

This thesis is arranged as follows. A feasibility study based on a literature review is described in Chapter II, providing guidelines for the definition of the target for this research, some notions are described on SMM, and a brief description of LPBF properties. Chapter III describes LPBF processes focusing on defects and process parameters; in Chapter IV and V respectively the aim of this research topic and experimental methods used for the characterization of SMM. In chapter VI results of the metallurgical and magnetic classification of materials are covered. Chapter VII presents the design optimization for the design of the electrical machine's rotor, while in Chapter VIII, a general discussion and conclusions of this work are presented and are proposed future developments of this research activities.

Chapter II. AM on E-Mobility

2.01 Introduction

This chapter is proposed to shed light on AM technology's potential for electrical machine constructions. We are starting with a summary of leading AM technologies nowadays available on the market and then a global vision of electrical machine types.

It will be done focus on materials in E-Mobility and the main components of an electric machine. An SYN RM machine rotor will be the best case of study for the testing potential of metal AM technologies, in particular LPBF processes. In conclusion, we will define the aim and novelty of this research.

2.02 Additive Manufacturing Technologies

The term additive processes identify all those processes that involve the construction of artifacts, from 3D models, by heating or melting the raw material, layer by layer. The born of additive manufacturing in 1987 corresponds to the commercialization of Stereolithography (SL) machines by 3D Systems. Initially, additive processes were used to build component models for prototyping, for this reason, it was also called rapid prototyping technology, products were primarily used to get a feel for the shape and exterior look. As the accuracy of existing processes improved, was possible to develop new materials to build functional components. Since 1987 an increasing number of technologies have been implemented, and with them, the companies involved in the design of machines, both to produce polymeric components and metal products.

Below we will briefly describe some of these technologies chosen from those most widely used commercially.

(1) The Basics principle

The fabrication of additive components involves numerous steps that may be more or less complex depending on the element and process chosen and may apply an iterative approach. Some of these steps can be considered common to all additive processes:

1. Design: The object intended to print is virtually created using any computed-aided design (CAD) software. During the design phase, the designer can implement freeform design strategies, such as topology optimization schemes. It's crucial to consider printer volume and orientation because these two constraints are stringent.
2. Conversion from CAD to the Standard Tessellation Language STL format (Figure 2). The CAD software normally converts and replaces the model's surface with a cloud of triangles.

   It's common occurring many errors during conversion, including:

a. Incoming direction of the vectors identifying each triangle: this implies an incorrect distinction between the inner and outer parts of the component.

b. Discontinuity between triangles.

c. Intersection between triangles.

Proper software for AM processes can manage STL files and include various tools for fixing them. Universally this type of software is called slicers and is necessary to manage/fix STL and orientate the part into a virtual machine volume, generating support structure, if required.

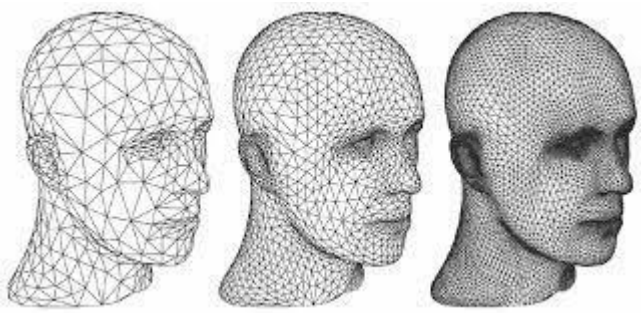

Figure 2 STL generation, from www.sculpteo.com

Once the part is well supported and oriented, the slicer will slice the virtual machine environment and prepare the file for etching every slice. During the etching stage are chosen manufacturing process parameters, layer height, speed, power, and distances between scan tracks. Different process parameter combinations can be set to obtain various properties, such as low surface roughness, high density, or productivity. The final conversion of layer path into machine language is done generating computer-aided manufacturing (CAM) file.

1. Loading the CAM file into the AM machine. Once CAM file is generated, it can be moved into the manufacturing machine environment. In this phase coping or adding and moving the part is possible for allowing multiple creation of different parts simultaneously.
2. Building. The machine will start the process creating the part layer-by-layer and, depending on the AM technology employed, the raw material can be powder or wire;
3. Part removal from the building platform. Supporting structures and parts will be detached from building platform.
4. Post-processing. This stage includes all processes after build, these can be heat treatment, milling, polishing.

The most widely used metal additive manufacturing technologies are listed here (Table 1 Map of main Meta AM Technologies), along with a brief description.

Deposition Method	Technologies	Processed Materials
Powder Bed	Laser Powder Bed Fusion LPBF	Maraging steels, stainless steels, Ti, Ti-alloys, Al- alloys, Ni-Ti, Co-Cr, Au, Ag,Inconel, Bronze Alloys, Cu- Alloys
	Electron Beam Melting EBM	Ti-6Al-4V, Ti-6Al-4V ELI, Ti Grade 2, Co-Cr
Directed Energy Deposition	Laser DED	Ti-, Ti-alloys, Inconel , Ta,W, Nb, Cu,, Cu-Ni, Steels,Al, Zircalloy

Table 1 Map of main Meta AM Technologies

(2) EBM - Electron Beam Melting

Arcam commercialized and developed, in 2001, the first Electron Beam Melting (EBM) machine. A scheme of EBM process is shown in Figure 4, high power electron beam is used as heat source to scan powder bed. First, a vacuum and then feeding helium in the process chamber are used to grant quality in the final parts. Stress reliefs are promoted keeping build platform at high temperature (600°C) in this way, in comparison to LPBF system, is possible to achieve microstructure with larger grain. Every layer is scanned twice, firstly using low current, granting a preheat and to achieve a partial melting of powder, secondly with high current to full melt the powder. With built rate of 70 mm^3 /s is one of the most productive system, despite high surface roughness due to spot size and layer high (Figure 3).

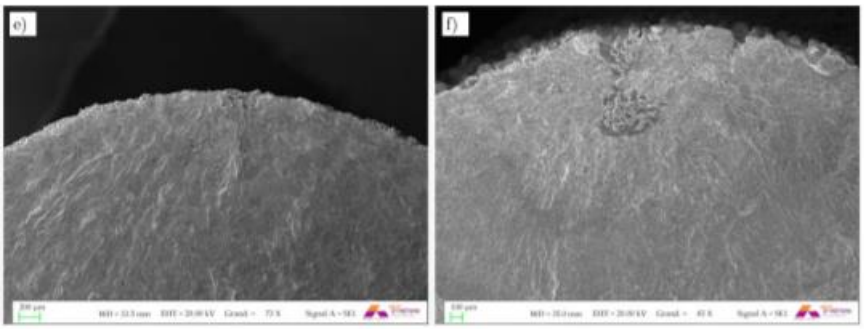

SLM EBM

Figure 3 surface roughness differences between LPBF and EBM process (Vayssette et al., *2018)*

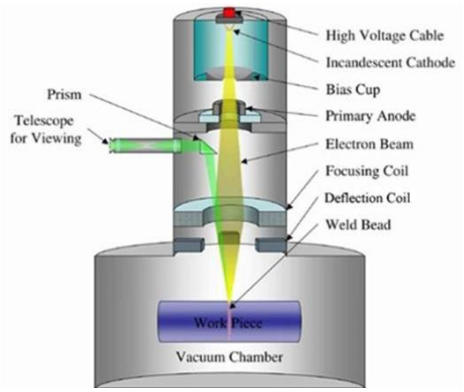

Figure 4 Electron Beam Melting (EBM) schematics from www.popular3dprinters.com/

(3) DED - Direct Energy Deposition

The DED uses wire or metal powder as raw material, which is deposited in the work chamber and simultaneously irradiated by the laser source (up to 20 kW infrared) to grant melting. Currently most commercial systems are sold to use powder, which leaks from one or more nozzles coaxial to the laser beam. Wire fed DED systems allow more efficient use of raw material but are more complex to control in real-time. This family of metal AM processes is one of the most productive, is possible to reach 4 g/s of deposition rate. In comparison to LPBF and EBM system microstructure have bigger grain due to higher spot sizes and higher power density during the process, lowering cooling rate speed.

(4) LPBF - Laser Powder Bed Fusion

In Laser Powder Bed Fusion (LPBF) a high power laser source (50W – 2 kW) provide heat source for raw material melting. To grant oxidation protection, oxygen is exhausted inflating gas protection like Nitrogen or Argon or Helium. Inert gas flow promotes both a constant surfaces cooling rate and evacuation of gasses and spattering, stress relief and cooling rates can be controlled using heated building platform (up to 400°C). In LPBF process, due to small laser spot sizes and localized heating/cooling sequences, stresses can increase over the ultimate strength threshold causing cracks (Figure 5). In addition, lower build rates, in comparison to DED or EBM, affects productivity.

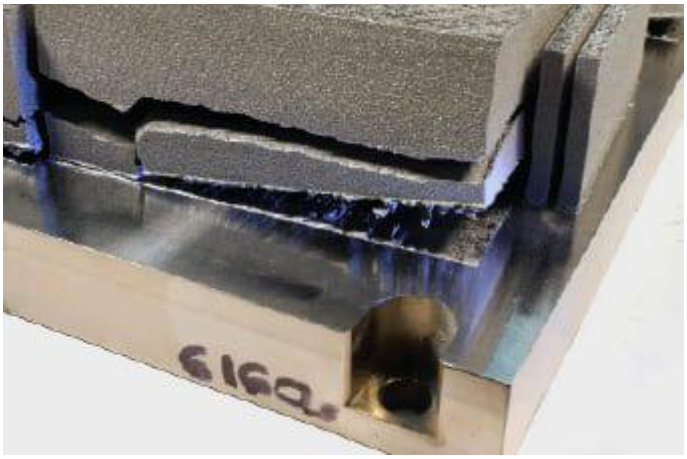

Figure 5 Part delamination due to crack formation and propagation, from (“Penn State CIMP-3D,” 2020).

2.03 Electrical Machine Construction and Design

(1) Construction

In an electric motor, stator and rotor are the basic elements acting (Figure 6). The stator, static part, will generate a rotating magnetic field, a composition electromagnetic vector. The rotor, rotating part, interact with electromagnetic field generating mechanical torque. A soft magnetic core is present in both, rotor and stator, amplifying magnetic field. An electric motor classification is made depending on interaction between magnetic field and rotor.

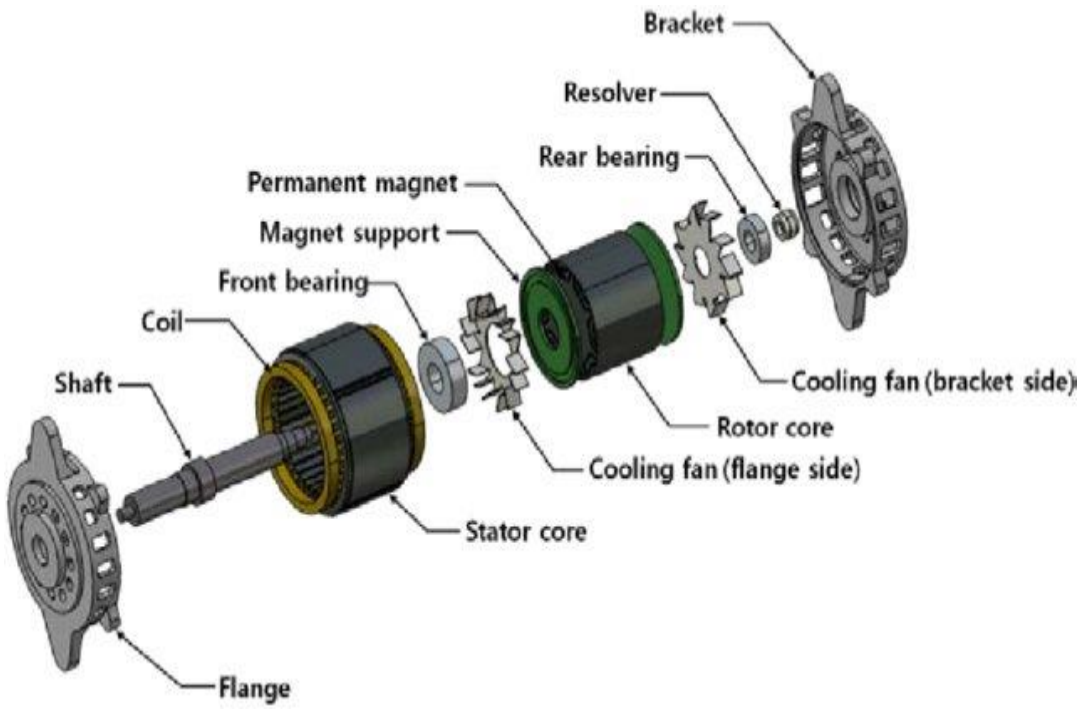

Figure 6 ISG motor scheme (Kim, 2013)

Two basic categories are based on relative position of rotor and magnetic field generated in the stator: synchronous if the position between both is locked during the rotation, otherwise asynchronous, rotor have a different rotational speed in comparison to stator's magnetic field.

The oldest forms of reluctance motor, a switched reluctance motor, was designed in

1838 and uses mechanical switches to control the motor speed. The motors could only revolve as rapidly as the switches could be manipulated using this switching arrangement. This was an extremely slow speed in the 1800s, when steam engines were still popular. The switching mechanisms improved throughout time, but the motors still had flaws, such as torque ripple causing irregular rotation speed. Direct current (DC) sources, such as batteries or rectifiers, can be used to power electric motors. Alternatively, alternating current (AC) sources like inverters, electric generators, or the power grid can be used (Table 2). Faraday's Law of Induction is the fundamental concept that governs the operation of an electrical motor.

Electric motors

DC Motors	AC Motors	Other Motors
DC Shunt Motor	Induction Motor	Stepper Motor
Separately Exited Motor	Synchronous motor	Brushless Motor
Series Motor		Hysteresis Motor
PMDC Motor		Reluctance Motor
Compound Motor		Universal Motor

Table 2 Types of electric motors

When an alternating current interacts with a changing magnetic field, a force is generated. The DC motor is the only one of the four basic types of motors that is powered by direct current. It's the most basic type of electric motor, with spinning torque created by current flowing via a conductor inside a magnetic field, the rest are all alternating current electric motors. The synchronous motor, which always operates at synchronous speed, is characterized by having rotor magnetically locked to the stator's revolving magnetic field and spins at the same speed. The frequency (f) and number of poles (P) are changed to change the speed of these devices, with $\omega_s = 120\ f/P$.

In another form of AC motor, the rotor conductors are cut by a rotating magnetic

field, resulting in circulating current in the short-circuited rotor conductors. The rotor begins to revolve and continues to rotate due to the interaction of the magnetic field and these circulating currents. This is an asynchronous induction motor that runs at a lower speed than its synchronous speed, with the rotating torque and speed governed by varying the slip, which gives the difference between synchronous speed ω_s and rotor speed ω_r (Equation 1):

Equation 1

$$Slip = \frac{\omega_s - \omega_r}{\omega_s}$$

It runs on the principle of EMF induction due to varying flux density. As a result, "induction machine" was coined.

In E-mobility the main requirements are efficiency, compactness, power density and reliability, the main categories in agree with these necessities are Synchronous reluctance machine (SynRM) and induction machine (IM) (Finken, Felden and Hameyer, 2008; Cao *et al.*, 2012; Galea *et al.*, 2014). Rotor of syn RM motors is made of soft magnetic core and his tendency to adjust its position according to minimum reluctance generate torque. Geometrical design and magnetic characteristics of materials used are the only variables to performances of the motor. In Figure 7 are shown different kind of rotors: a salient pole DC, b PM surface mount, c Synchronous reluctance, d switched reluctance.

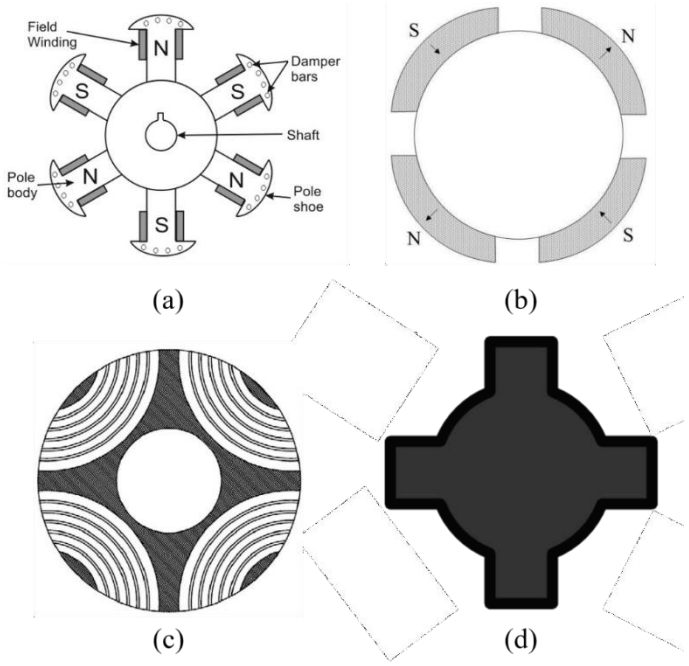

Figure 7 The cross-sections of four typical rotor topologies: (a) salient pole DC with armature windings, (b) Surface-Mount Permanent Magnet (PM), (c) Synchronous Reluctance (SyR), (d) Switched Reluctance (SR). Artwork adapted from steemit.com/.

(2) Design

In electric motor, desired electromagnetic performances, e.g. in terms of power and torque, are obtained optimizing part's dimensions. Traditionally an analytical method was used to approach the problem but more recently mathematical optimization technique has established, for both technique is required a starting design as template, defining dimensions of final motor.

Geometrical design highly influences performances of magnetic cores and represent a wide part of total EM weight. Metal AM can improve power to weight ratio optimizing shapes of heavier parts and grant a freedom in the design, allowing 3D core design modification. These advantages are counterbalanced by lower productivity and higher costs of AM technologies, compared to traditional lamination punching or powder pressing. Optimize and facilitate production must be take into account during design process, more than ever in, relatively new, AM processes. Considering LPBF is not suitable for thin sheet electrical steel stacking,

the optimal solution is proceeding from a typical design and, then, optimizing shapes considering mechanical and magnetic properties of AM products.

After the above-mentioned consideration, two ways are possible: use pure iron, granting a full dense crack-free specimen or use electric steel (silicon iron alloy), granting better magnetic performances despite processability. Considering minimal flux variation in the rotor, syn RM machines appear to have a good compatibility for AM technologies. The rotor is composed only of SMM and can be bulk instead stacked.

2.04 Soft Magnetic Materials - SMM

Components inside an Syn RM motor are mostly made of SMM. This class of materials is characterized to lose completely their magnetization if magnetic field applied is equal to zero. Contrariwise this generates an induction-applied field loop, also known as B-H loop, an example in Figure 8.

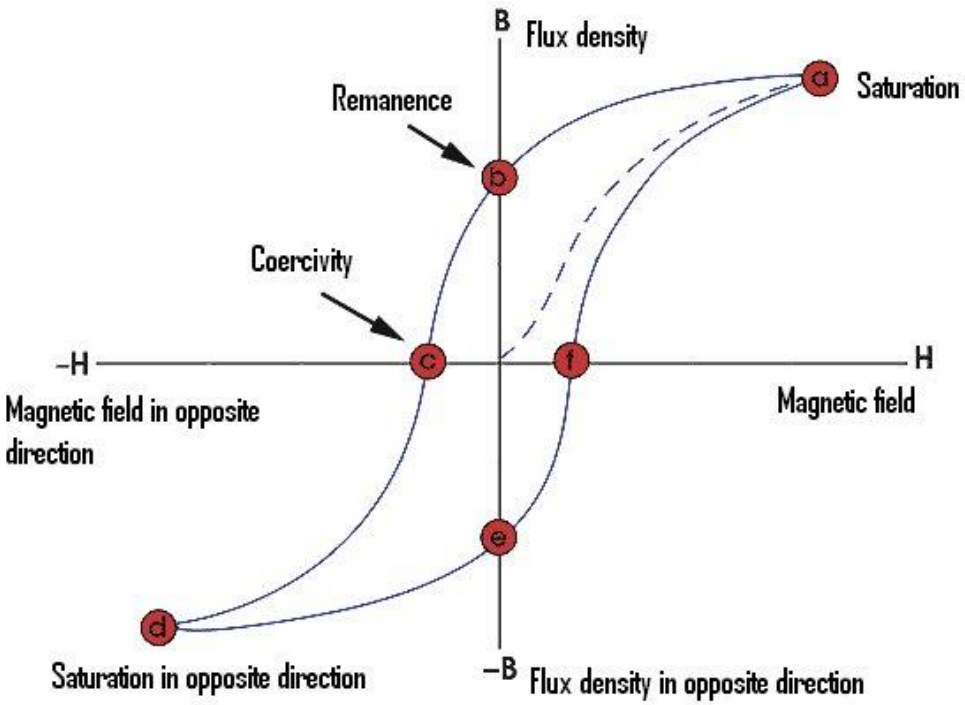

Figure 8 Typical B-H loop of a ferromagnetic material. (Chukwuchekwa, 2011)

Following properties characterize a good SMM for EM application:

- High μ, permeability, increase efficiency (high inductions *B* at low applied field *H*)
- High saturation, grant to reach higher *B* increasing the torque.
- Low coercivity, reduces hysteresis losses (*B*-*H* loop area).
- High resistivity, limit eddy currents propagation induced by *B* frequency, reducing power losses joule heating due to joule heating.

Figure 9 represent typical value of magnetic properties of most known SMM.

	Composition (wt% cryst. alloys, at% amorphous alloys)	Max. relative permeability (μ_{max})	Coercive field H_c (A/m)	Saturation polarization J_s (T)	Curie temperature T_c (°C)	Saturation magnetostriction $\lambda_s = (\Delta l/l)_{Js}$
Polycrystalline Fe	Fe_{100}	$3–50 \times 10^3$	10–100	2.16	770	5×10^{-6}
NO Fe–Si	$Fe_{96\text{-}99}\text{-}Si_{1–4}$	$3–10 \times 10^3$	30–80	1.96–2.12	735–765	10×10^{-6}
GO Fe–Si	$Fe_{97}\text{-}Si_3$	$15–80 \times 10^3$	4–15	2.02	750	$1–3 \times 10^{-6}$
Fe–(6.5 wt%)Si	$Fe_{93.5}Si_{6.5}$	$5–30 \times 10^3$	10–40	1.80	690	5×10^{-7}
Sintered/bonded powders	$Fe_{99.5}P_{0.5}$	$10^2–10^3$	100–500	1.65–1.95	770	—
Permalloy/Mumetall	$Fe_{15}Ni_{80}Mo_5$/ $Fe_{14}Ni_{77}Mo_4Cu_5$	5×10^5	0.3–2	0.75–0.80	420	1×10^{-6}
Permendur	$Fe_{49}Co_{49}V_2$	2×10^3	30–100	2.35	930	$60 \cdot 10^{-6}$
Fe50–Ni50	$Fe_{52}Ni_{48}$	10^5	4	1.60	450	25×10^{-6}
Sintered ferrites	$(Mn,Zn)O \cdot Fe_2O_3$	$10^3–10^4$	5–20	0.4–0.55	130–280	-2×10^{-6}
	$(Ni,Zn)O \cdot Fe_2O_3$	$10^2–10^3$	20–200	0.2–0.35	110–400	-20×10^{-6}
Sendust	$Fe_{85}Si_{9.5}Al_{5.5}$	50×10^3	5–10	1.70	670	1×10^{-6}
Amorphous alloys (Fe-based)	$Fe_{78}B_{13}Si_9$	10^5	2–5	1.56	415	37×10^{-6}
Amorphous alloys (Co-based)	$Co_{67}Fe_4B_{14.5}Si_{14.5}$	5×10^5	0.5–1	0.62	320	5×10^{-7}
Nanocrystalline alloys (FINEMET)	$Fe_{73.5}Cu_1Nb_3Si_{13.5}B_9$	5×10^5	0.5–1	1.24	600	2×10^{-6}
Nanocrystalline alloys (NANOPERM)	$Fe_{86}Cu_1Zr_7B_6$	5×10^4	3	1.52	600	1×10^{-7}

Figure 9 Representative Soft Magnetic Materials and Typical Values of Some Basic Magnetic Parameters at Room Temperature. (Fiorillo et al.*, 2016)*

Using solid structure is possible where the rotor flux variation is minimal granting a better solution instead lamination stacking and maximizing mechanical integrity. To minimize propagation of eddy currents are used 0.1 to 1 mm thick insulated sheet stacked together, in this way mechanical integrity is lower.

SMM available on the market as powder are listed in sections from (I) to (III).

(1) Pure Iron (Fe)

Pure iron was widely used in the past for his properties, such as electrical conductivity and magnetic permeability. Depending on purity, a high purity iron can reach high magnetic saturation, low coercivity, high permeability, as well as excellent conductivity, especially in medium induction ranges.

(2) Iron-silicon alloys (Fe-Si, or silicon steels)

Nowadays the most common solution is alloying Fe with Si in the concentration range 3 - 6 % wt., granting a good electromagnetic property: low hysteresis losses, high resistivity, high permeability, also called electrical steel, laminated Fe-Si alloys.

(3) Materials Considerations

Considering the list of material beforementioned on Figure 9 an high resistivity should be preferred to limit power losses. The choice of a range of materials is related to performances but also to good processability. Electrical steels and pure iron can represent excellent candidates considering performances of Fe-Si alloy and processability of pure iron.

Chapter III. Laser Powder Bed Fusion - LPBF

3.01 Introduction

Laser Powder Bed Fusion (LPBF) is a manufacturing process, with high level of automation and complexity, inside metal powder additive manufacturing categories. The mechanism behind laser interaction with powder, creating a melt pool, and his stability are the basis for comprehension of microstructure and defects. Next chapter will explore the notions to interpret this phenomenon.

3.02 Melt Pool generation

In LPBF system the heat source is moving fast and interact with powder bed, generating the melting process. The results are rapid heating and melting of raw material, leading melt pool formation and generating heat affected zone (HAZ), as represented in Figure 10

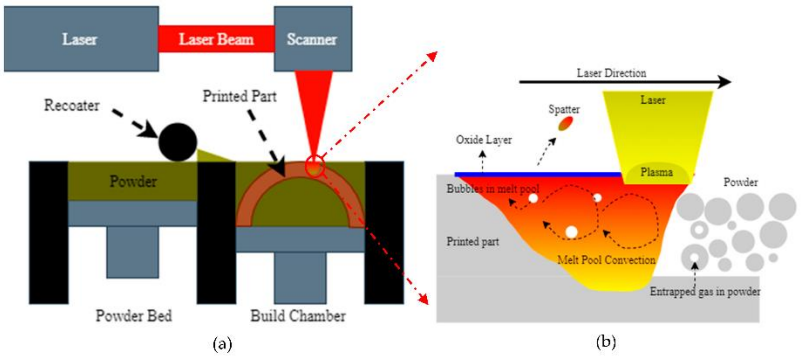

Figure 10 (a) Schematic diagram of L-PBF process, (b) Laser–melt interaction region (Yadav et al., *2020)*

Low energy laser scenario is represented by incomplete melting and bonding of melt

pool, high surface tension during liquid state generating large and irregular voids (Vrancken *et al.*, 2014; Simonelli *et al.*, 2015). Balling phenomenon is as well related to surface tension, preventing the liquid from wetting substrate and generating irregular surface. Other phenomenon related to surface tension of melt pool are Plateau-Rayleigh instabilities, when the length to width ratio is too high compared to liquid viscosity, molten track breaks into spherical particles, as shown in Figure 11 (Kruth *et al.*, 2004)

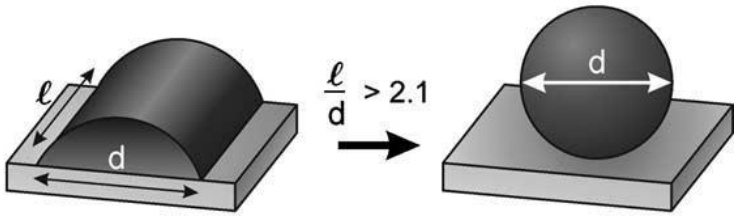

Figure 11 Sketch adapted from (Kruth et al.*, 2004), showing the break-up of a half-cylindrical track into a number of spheroids when its length-to-width ratio is too high, according to Plateau- Rayleigh theory.*

Another phenomenon related to thermal gradients and surface tension gradients is Marangoni effect. Well known in welding processes (David, Babu and Vitek, 2003), surface tension depends to temperature and alloy composition, this will generate radial convective flows inside melt pool (Figure 12) resulting in a deeper shape if outwards, that lends itself more easily to balling, otherwise the shape is shallower (Rombouts *et al.*, 2006).

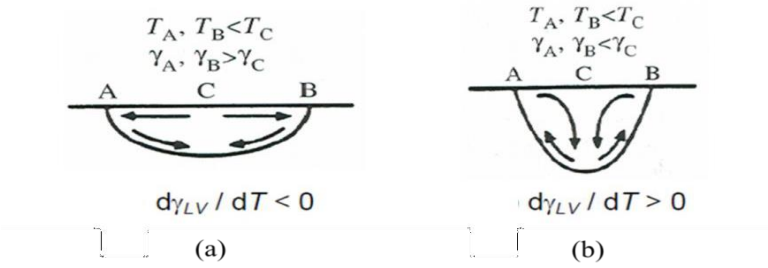

Figure 12 Surface tension gradient-induced capillary flows in the melt-pool can be directed radially outward (a) or inward (b), depending on whether the variation of the surface tension with temperature is negative or positive, respectively. Adapted from (Kruth et al.*, 2010).*

Another phenomenon related to melt pool generation is, keyhole, well known in laser welding literature. Evaporation of powder particles generate a recoil pressure, due to high intensity of laser power density, change melt pool shape from flat to protuberant, generating a turbulent flow. In LPBF low recoil pressure promote layer flattening granting better powder deposition, when pressure become higher the material is expelled generating porosities. Once cool these porosities can be small and spherical typical of gas bobble, or irregularly shaped if laser energy density is too low (Figure 13).

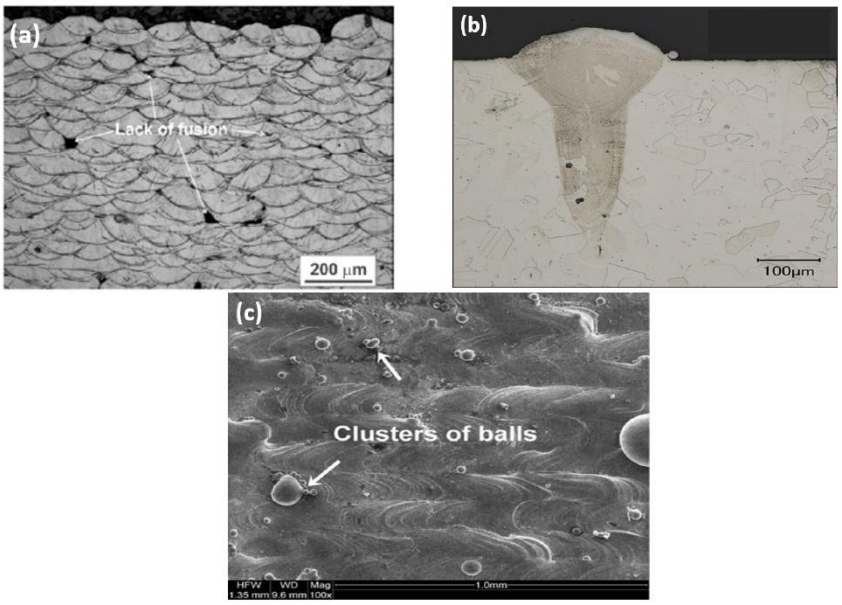

Figure 13 Figure (a) Micrograph showing lack of fusion pores; (b) keyhole porosity; (c) balling defect.; ((King et al.*, 2014; Zhang* et al.*, 2016))*

A powder cinematic phenomenon is bed denudation, a combination of surface tension and recoil pressure. Both case, high and low recoil pressure can generate denudation (Figure 14), but the worst-case scenario is when is low, in that case metal vapor can expand into a wide plume expelling particles.

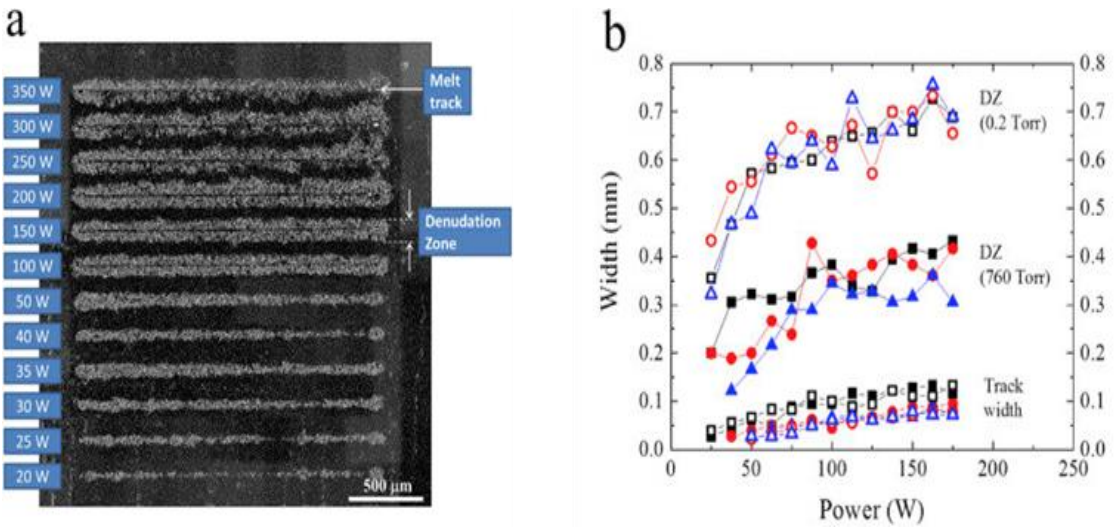

Figure 14 Powder denudation phenomenon in SLM. (a) Wide field image of denuded zones around melt tracks created by LPBF as a function of laser power and at a scan rate of 2 m/s. (b) Measured denudation zone (DZ) and resolidified track widths as a function of laser power, scan rate and ambient Ar pressure.. ((Matthews et al.*, 2016))*

3.03 Defects and residual stresses

Another important phenomenon, determining good or bad quality of produced parts, is related to applying high heat energy density in a very short time interval (µs order). Around laser spot the poor heat conductivity of powder generate strong thermal gradient generating non uniform heat affected zone (HAZ). During heat this region tend to expand, but blocked by surrounding metal, is plastically compressed. During cooling, underlined layers are contract by upper layer, generating tensile residual stresses, this mechanism is known as temperature gradient mechanism (TMG) (Figure 15). If residual stresses locally reach the ultimate tensile strength a crack can occur.

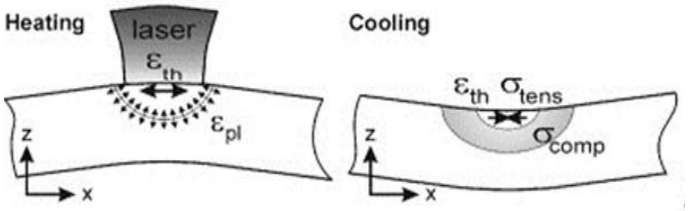

Figure 15 The two phases in the temperature gradient mechanism (TMG)

From literature measure and predict residual stresses is important to prevent part failure, there are different strategies to evaluate it, destructive and nondestructive, direct, and indirect. X-ray diffraction, hole drilling and sample deflection measurement are the mostly used. Otherwise, important is numerical analysis to predict this phenomenon, using finite element method, and minimize it during design stage.

3.04 Microstructure in LPBF

Microstructure in laser powder bed fusion processes is dependent by geometrical, thermodynamic and kinetic factors, generating two regions, the melt pool and, around it, where diffusion-based transformation are generated by temperature sufficiently high, the heat affected zone (HAZ)

Solidification front is perpendicular to melt pool boundary, determining thermal gradient direction, and so, melt pool shape. Detailing this phenomenon, a local solidification front is generated in melt pool causing different consequences in grains typologies, can be found columnar grains, near HAZ, or equi axed grans in the center line of melt pool, depending not only by thermal gradient, but also to main nucleation method.

Solidification structure type, cellular, planar or dendritic depend mainly by cooling rate and chemical composition of alloy. Planar structures are obtained during stable interface positive temperature gradient, without differences in local chemical composition. If the interface become unstable according to super-cooling a planar structure is not possible instead cellular or dendritic, depending on segregation in the liquid phase.

The solidification type and grain structure depend by two parameters: G thermal gradient and R front speed, the ratio between these two elements (G/R) define the morphology of grain structure. With low value occurs planar solidification, beside at high value the structure is equiaxed dendritic; a solidification map is visualized in Figure 16 and can be used to predict grain morphologies and solidification modalities.

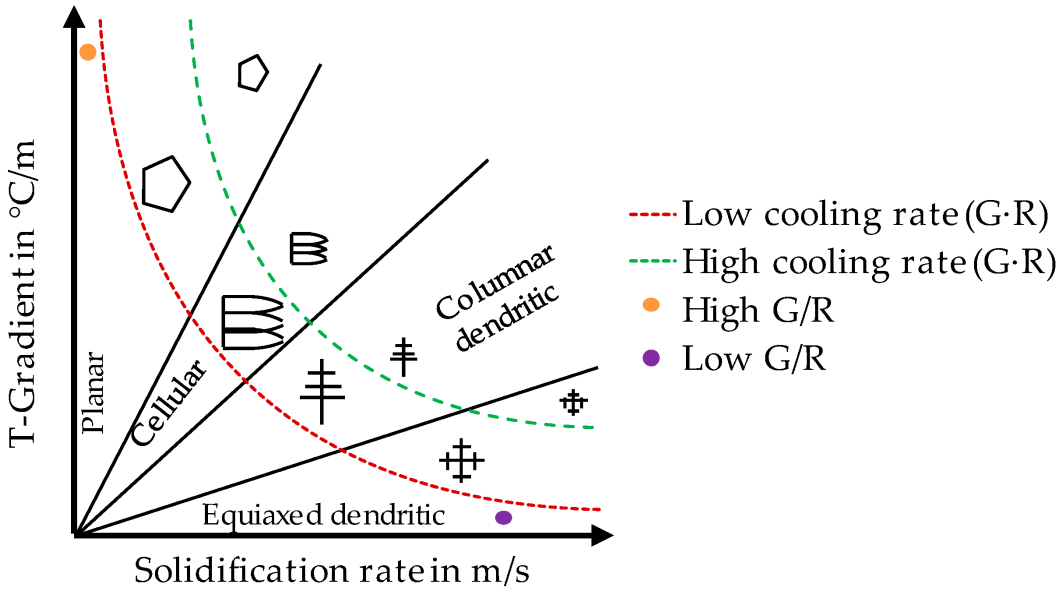

Figure 16 Effect of temperature gradient G and solidification rate R on the morphology and size of the solidification microstructure, from (Fujieda et al.*, 2017)*

In LPBF processes, differentially to welding process, an overlap between adjacent scan tracks and layers increases difficulties in results interpretation. However, a constant remelting of generated melt pool occurs, originating an analogy between build direction and columnar grain growth direction.

3.05 Process parameters effects

Below, we'll go over some of the most significant LPBF processing factors, such as laser power, scan speed, hatch spacing, layer thickness, laser energy density, and scan pattern techniques, and how these affect component quality, microstructure, and behavior. Interactions between the processing parameters listed above are also explored.

(1) Laser Power

Laser power is the simplest parameter promoting samples densification, but

depending on materials involved, reaching a maximum value above which melt pool stability is compromised. Increasing power will promote bounding of layers and scan tracks, generate a deeper interaction between laser and powder, rising wettability. An excessive power induce vaporization, usually unwanted, but in some cases can reduce balling generating less defective sample. Another phenomenon related to power, but more generally to thermal gradients, is a strong attitude to epitaxial growth of grains along the build direction, increasing power will generate strong thermal gradients capable of that.

(2) Laser Scan Speed

Power (P) and speed (v) of laser source are the main process parameter involved in melt pool generation and the ratio (P/v) represent the linear energy density (LED). The scan speed, in the opposite way of the power, increase width and dept of scan track if decreased. LED is a fundamental parameter to study melt pool stability (Figure 17) and, introducing layer thickness and distances between tracks, for part densification.

At low and high ratio of LED can be find an irregular melt pool, causing process instability. High value at low power generates a bigger HAZ creating bigger and irregular melt pool. In the opposite way, LED low, not enough energy is promoting powder particle melting resulting in an fragmented melt pool. Medium value of LED grant a stable melt pool Figure 17.

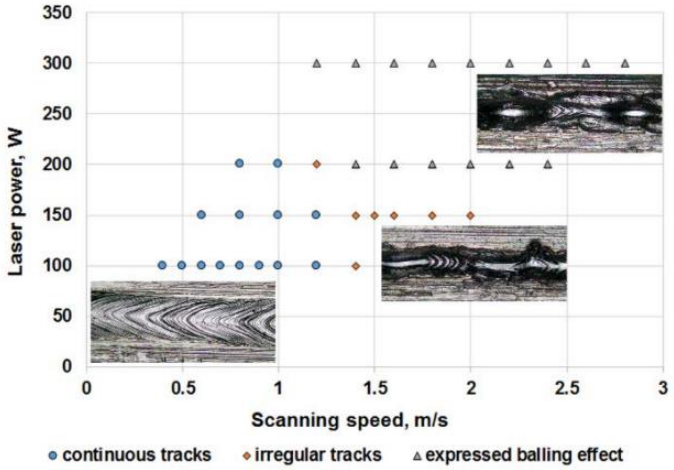

Figure 17 Process map obtained on the 100–300 W laser power and 80 µm laser spot diameter ("low-power system") from (Makoana et al., *2018).*

(3) Hatch Spacing

The distance between centerline of the adjacent laser tracks correspond to hatch spacing. Also, this process parameter has is role in sample's densification by overlapping scan track. Less hatch distance, so more overlapping, increase density; it is not correct to adopt too much overlap to avoid linear voids related to denudation effect and to decrease thermal gradients and so residual stresses. A correct way to define it is by measuring melt pool dimension, once fixed laser power and speed, and define how much overlap is needed to avoid un-melted zone Figure 18.

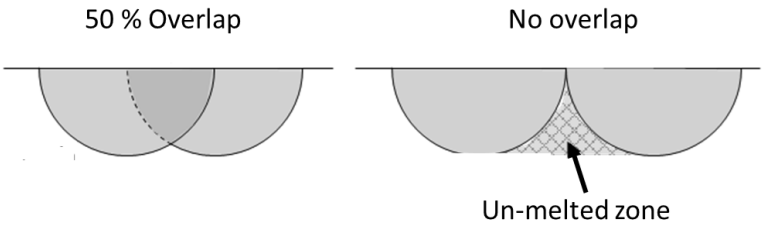

Figure 18 Hatch spacing

(4) Layer Thickness

Last process parameter is layer thickness, increasing layer high correspond to improved productivity but on the other hand higher surface roughness, due to more powder available for spattering, and more volume of powder to change state from solid to liquid. Generally, a higher layer thickness reduces residual stresses lowering thermal gradient during production.

(5) Volume Energy Density

Combining all the parameters above mentioned can be useful to consider the amount of laser input energy per material in volume unit. The common expression for volume energy density (*VED*) is the following (Equation 2):

Equation 2

$$VED = \frac{P}{v \cdot t \cdot h}$$

P is laser power, *v* the scan speed, *t* layer thickness and *h* is the hatch distance, in case of single track the *h* is substitute with laser spot *s.*

In a recent paper (Thomas, Baxter and Todd, 2016), a normalized process mapping approach is proposed, in which an optimal design window is discovered inside the space defined by two sets of dimensionless process variables, namely the hatch spacing and the single-track volumetric laser energy density. The authors demonstrated that by making dimensionless both the energy density and the hatch spacing using the alloys' density and thermal properties (thermal conductivity, heat capacity, and melting temperature), a normalized equivalent energy density *E0** can be calculated by dividing the dimensionless quantities.

The equation in has been proven to be proportional to this quantity (Figure 19). Importantly, regardless of the particular processing parameters employed, a constant

value of *E0** will give an equally energy efficient treatment during powder bed AM, and so constitutes a helpful tool for process optimization. The authors also show that differing E0* values result in distinct melt-pool geometries and, as a result, diverse microstructures, which might result in highly varied functional behaviors (e.g., different tensile properties).

Figure 19 depicts the normalized process map presented in (Thomas, Baxter and Todd, 2016), in which the points in the processing space were derived from literature data for various alloys and AM powder-based techniques. The graphics show the E0* isopleths and processability ranges.

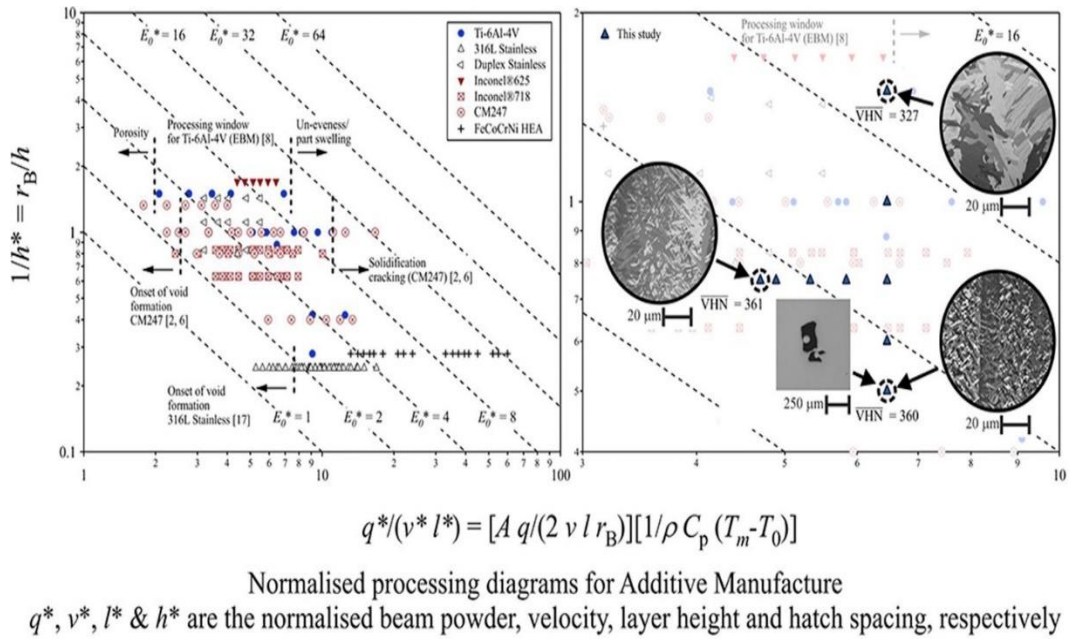

Figure 19 Normalised processing diagram for AM, from (Thomas, Baxter and Todd, 2016).

(6) Laser Scan Strategy

The method used to create scan patterns on the powder bed has a significant impact on the development of residual stress, and so, on deformations. Figure 20 depicts the most popular scanning patterns.

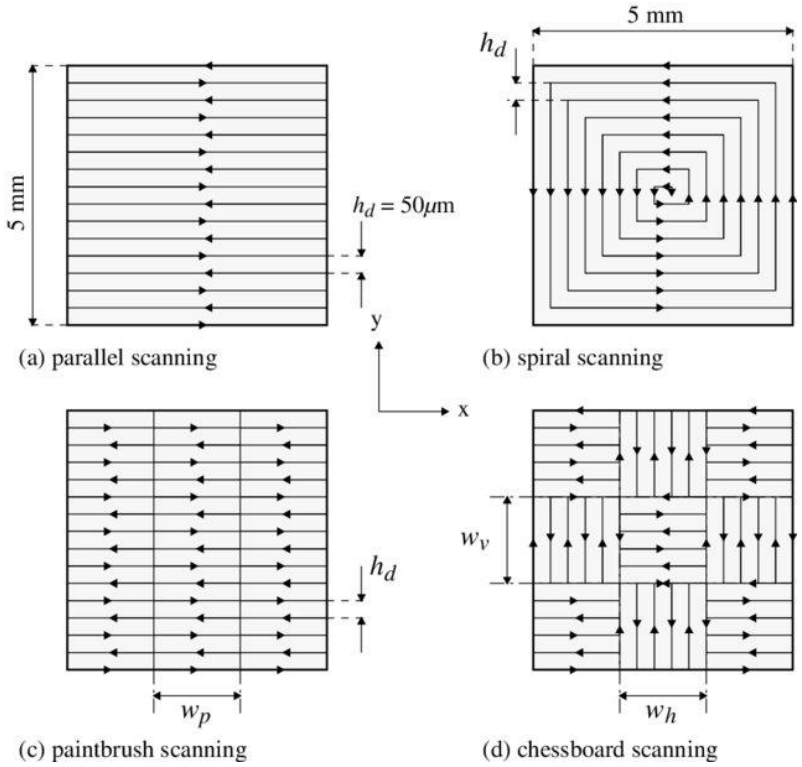

Figure 20 four scanning strategies from (Jhabvala et al.*, 2010)*

The authors of (Kruth *et al.*, 2004), who studied a wide range of the most prevalent pattern methods, indicate that sector-based solutions should be favored to reduce heat stress. The consecutive sector method, in particular, offers the advantage of minimizing temperature gradients. Short scan vectors minimize residual stress produced during the LPBF process, according to recent numerical simulations employing a Ti-6Al-4V thermomechanical model (Parry, Ashcroft and Wildman, 2016).

Exotic methods such as spiral (Nickel, Barnett and Prinz, 2001; Jhabvala *et al.*, 2010) and fractal patterns (Catchpole-Smith *et al.*, 2017) might possibly give advantages in stabilizing temperature gradients and reducing residual stresses, but they can be difficult to achieve for particular component geometries. It was demonstrated in (Thijs *et al.*, 2013) that altering the scan method changes the crystallographic texture of AlSi10Mg. The authors demonstrated that utilizing scan vectors rotated by 90 degrees inside and across layers, a strong fiber texture generated by scanning each layer with unidirectional vectors could be transformed into a weak cube texture.

Chapter IV. Research Scope, Aim and Novelty

4.01 Research Scope

Based on the literature research done in this chapter, the present research's scope is defined. The soft magnetic core is chosen over permanent magnets as the optimal alternative for development using powder bed fusion AM process due to the former's lower material prices and availability, especially when compared to rare earth-based permanent magnets.

High-silicon steel, i.e. Fe-Si alloy with Si content about 3% and pure iron, are chosen as the raw material due to high electrical resistivity, which helps counteract eddy currents, strong magnetic properties, and good raw material availability.

Pure iron magnetic properties are lower in comparison to Fe-Si alloy, but it is easier to process using a laser source.

Furthermore, due to its limited workability, the silicon iron alloy is an excellent choice for showcasing the advantages of tool-free production over traditional methods.

LPBF can create geometrical features with better resolution and lower surface roughness than other AM processes thanks to the smaller beam spot size and layer thickness. This benefit of LPBF is particularly important since it reduces the needs for part post-processing, which can be time-consuming and costly, if access to the surfaces is restricted due to the part's geometrical complexity.

Finally, we recognize that achieving the full potential of additive fabrication in electrical machine production would need simultaneous, product and process developments. As a result, this thesis also addresses rotor core design optimization. FEM analysis is the best consolidated tool for component design, since it is undoubtedly the most powerful design tool to match the design for additive manufacturing.

The goal of this research is to improve the torque to power density of a synchronous electrical machine (Syn RM) by optimizing the rotor's core considering three-

dimensional geometry design and using LPBF technology to produce functional prototype in soft magnetic high-silicon steel, which was also developed as part of this research. By achieving this aim, AM powder-bed technology will be able to demonstrate its relevance and advantages in the creation of electrical gear.

4.02 Research Novelty

The suggested research is new in two ways, according to the author's understanding. First, no attempt has ever been made in the literature comparing pure iron and silicon iron alloy for electromechanical purposes using AM technique. Second, there has never been any discussion of using FEM based modeling to build real-world rotor cores considering AM as manufacturing process. The above-mentioned improvements are made possible by achieving intermediate research objectives, which track progress toward the goal.

4.03 Research Objectives

The following are the study goals, which are summarized in:

- Investigate if LPBF can be utilized to process soft magnetic materials for the production of electrical motor parts: Determine which processing and post-processing settings provide the optimum material characteristics based on the desired performance (mechanical or magnetic).

- Investigate the possibility of improving the performance of a synchronous rotor core by developing 3D designs free of manufacturing constraints: Improving the torque-to-weight ratio of an electromechanical component while maintaining structural integrity; putting the suggested approach to the test in two and three dimensions on the case study of choice. The latter should be a pre-existing synchronous rotor core design. The magnetic properties of the 3D-printed material are taken into account during the design process, and the results are compared to the original design to show how the design approach and material

properties affect device performance.

- Manufacturing of the final rotor design: Once the aforementioned set of requirements has been satisfied, the next step is to use LPBF to construct the designed rotor. The prototype will be utilized in future research to experimentally evaluate the proposed solution's electromechanical performance and to provide a direct comparison to traditionally manufactured equivalents.

Chapter V. Experimental Methods

5.01 Introduction

The experimental methodology adopted for this research will be described in this chapter, in addition of manufacture and characterization of pure iron and silicon iron alloy samples produced by LPBF. First, a description of the LPBF system, raw material powder, and sample varieties created is presented. The material processing (LPBF parameter settings) and post-processing (heat-treatment temperatures and durations) techniques are then described. Finally, the experimental procedures utilized to characterize the metallurgical, mechanical, and magnetic characteristics of the samples are explained, as well as the steps used to prepare the samples for characterization.

5.02 Powder

In the present work, a commercial-purity iron (hereafter indicated as Fe) and an iron-silicon alloy with a 3wt.% Si content (hereafter indicated as Fe-Si3) were investigated. Gas Atomized (GA) powders with a particle size in the range of 15 – 45 µm, were supplied by TLS Techinik GmbH and used as raw material for this study. Chemical composition and granulometry of feedstock powders is summarized in Table 3.

Element	**Fe**	**Si**	**C**	**Mn**
Pure iron	99,8	0,011	0,007	0,017
FeSi3	96,7%	2,92%	0,01	0,17
Fe D10	10.54 um		**FeSi3 D10**	12.16 um
Fe D50	28.79 um		**FeSi3 D50**	30.26 um
Fe D90	53.23 um		**FeSi3 D90**	47.59 um

Table 3 Powder chemical composition and grain dimension

In order to avoid particle adhesion and improve the flowability, powders were subjected to a low temperature drying process before the L-PBF process performed for 3h at 60°C in oven and then sieved in 230 mesh sieves.

5.03 LPBF Machine

All the specimens were built by using SISMA MYSINT100RM system, a LPBF machine equipped with a Trumph fiber laser source (wavelength 1030 nm, 50 μm of spot diameter, maximum power of 200 W, 175W on build plate), technical specification on Table 4. The manufacturing process was performed under nitrogen inert gas and a 0.1% content of residual oxygen inside the working chamber. The inert gas flow speed was set at 2 m/s. The Materialise Autofab software was used for specimen's orientation on the building plate, to create the support structures and define the process parameters. Specimens were built using a roto-translating chessboard scanning strategy (3x3 mm^2 chess). All of the builds took place on a mild steel platform and the powder levelling system consists of a rubber x-lip level bar.

SISMA MYSINT 100 RM Technical Specifications	
Build platform Diameter (mm)	100
Maximum Build Height (mm)	100
Layer Thickness (um)	20-50

Table 4 Technical specification of LPBF System Sisma Mysint 100 RM

5.04 Sample Types and process parameters

For each powder, process parameters were optimized by randomly distributing 32 samples (10x10 mm base, 15 mm height) on the construction plate at various values of laser power P [W], scan speed v_{scan} [mm/s], and hatch distance h [mm]. The thickness of the layer t was fixed at 0.02 mm. Table 5 illustrates the process parameter combinations that were studied and in Figure 21 the density sample distribution. A second experimental test plan for pure iron was carried out to examine a lower scan speed rate in order to locate a peak in the density value previously obtained in FeSi3 during the first test plan.

The density of the specimen was determined using an analytical balance and a non-destructive gravimetric technique according to ASTM B962 (0.0001 g precision) ("ASTM B962 ," 2020). The ratio between the observed density and the reference density for pure iron (7.87 g/cm3) (*ASM Handbook Vol. 2: Properties and Selection: Nonferrous Alloys and Special Purpose Materials (ASM Int.) 10 Ed., 1990*, 1990) and a 3 wt. percent Si iron-silicon alloy (7.65 g/cm3) was used to calculate the relative density [percent]. For the determination of the optimal set of process parameters, a density of 99 percent was established as a minimum. The placement of specimens on the building plate is described in detail in Figure 21.

POWER [W]	**Scan Velocity [mm/s]**	**Hatch Distance [mm]**	**Layer thickness [mm]**
100	500	0.1	0.02
120	700	0.07	
145	900		
170	1100		

Table 5 Summary of the investigated combination of process parameters

Specimens used for process optimizing were also subjected to metallographic analysis, roughness and hardness tests.

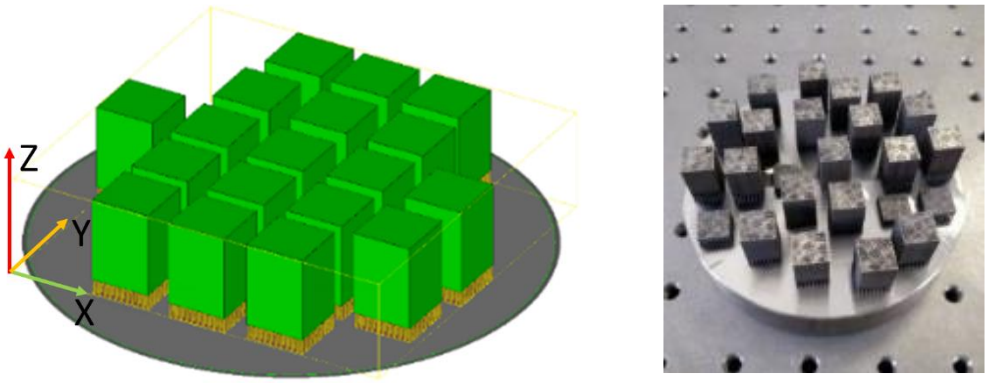

a b

Figure 21 Example of layout of specimens for process optimization (a). Specimens for process optimization in pure iron (b).

The set of process parameters chosen as optimal was used to produce eight specimens for tensile tests consistent with ISO 6892-1 (“ISO 6892-1,” 2020), which geometry is shown in Figure 22-a. All specimens were produced with the axis parallel to the Building Direction, as depicted in Figure 21-b. Influence of sample orientation on microstructure, mechanical and magnetic properties will be evaluated in further analyses, since the aim of the present work is to evaluate only the influence of heat treatment conditions. After the process, four of the eight specimens underwent an annealing heat treatment at 850 °C per 1 hour to relief residual stresses. The annealing temperature was chosen in order to prevent any phase transformation during the treatment or upon cooling to room temperature. Heat treated specimens are hereafter indicated as “HT”, in opposition to “AB” specimens tested in the As Built condition without the application of any post process heat treatment. Tensile tests at room temperature were performed according to ISO 6892-1 (“ISO 6892-1,” 2020) using a Italsigma hydraulic testing machine equipped with a 100 kN load cell.

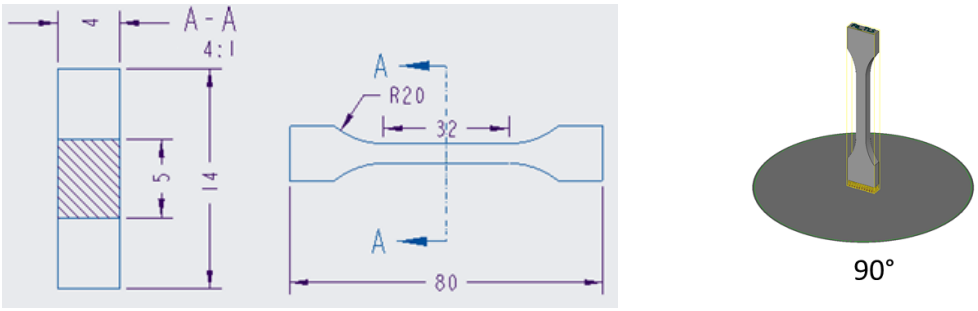

a b

Figure 22 Geometry of the tensile specimens (a), schematic representation of specimen orientation during the building process (b).

Vickers Hardness measurements with 0.2 kg load (HV0.2) and 15 s of dwell time were carried out in according to ISO6507 standard ("ISO6507 ," 2020). The hardness variation was evaluated in the build direction (Figure 23) both on AB and HT samples.

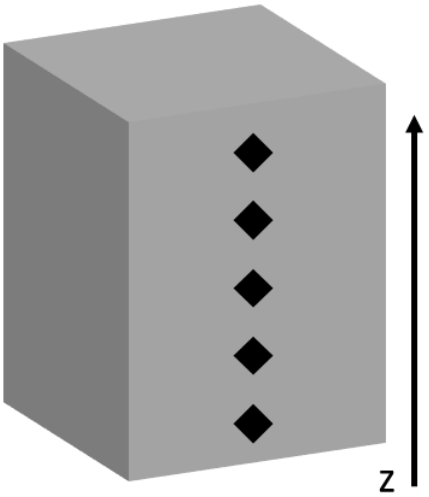

Figure 23 Hardness measurements preformed along build direction z

The microstructure of as built and annealed specimens was investigated through OM microscopy on polished and etched (3% vol. HNO_3) cross sections. Both scan plane

and build plane sections were investigated.

Magnetic properties were evaluated in terms of first magnetization curve and relative permeability. Four Toroid sample 80x70x5mm (Figure 24) were build, two of pure Iron and two of Silicon 3% Iron alloy. For each material, one sample was annealed in order to evaluate how residual stresses and microstructure influences magnetic properties.

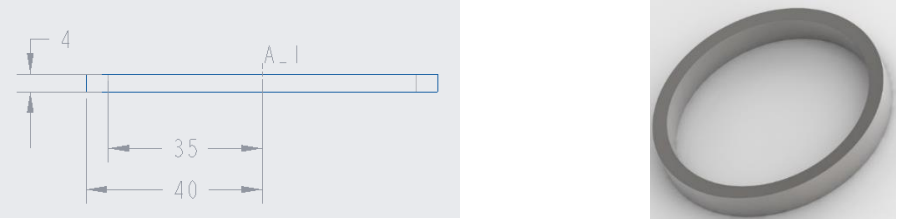

a b

Figure 24 Sample geometry of the specimen for magnetic characterization

The ring samples were constructed with their bases parallel to the construction platform, as illustrated. The benefits of adopting this orientation for the ring samples are multifold: the first is that it allows us to reduce the number of auxiliary structures and, as a result, the amount of post-processing required. We may measure the magnetic characteristics of the material in its plane of isotropy by constructing the ring samples with their bases parallel to the horizontal plane.

5.05 Heat-Treatment of the Manufactured Parts

To assess the impact of a post-measure heat treatment on the microstructure, mechanical and attractive properties of L-PBF tests, a pressure alleviation heat treatment at 850 °C for 1 hour followed via air cooling was performed. Tests exposed to the hotness treatment were recognized as "HT", contrary to the L-PBF As-Built (AB) ones. The hotness treatment temperature (850 °C) was picked fully intent on diminishing the leftover pressure and lessening the thickness of disengagements, while keeping away from the stage change from α-Fe to γ-Fe at 911

°C and the ensuing recrystallization, to hold the high mechanical strength coming about because of the L-PBF measure. Truth be told, in (Letenneur, Kreitcberg and Brailovski, 2019) it was shown that a strengthening in the γ-Fe locale (1300 °C) prompted a sensational drop in the mechanical strength of unadulterated iron produced by L-PBF contrasted with the As-Built condition and to the material pressure diminished at 650 °C, beneath the α-Fe to γ-Fe stage change.

The impact of annealing temperature on the microstructural development and magnetic characteristics of LPBF high-silicon steel was also studied. As a result, cubic and ring specimens were annealed for 1 hour at two temperatures, 750 °C and 850 °C, before being cooled in the furnace. The experiments were carried out on samples generated at set processing parameters, which were designed to offer a good balance between minimal fracture development and low porosity in the parts.

5.06 Sample Preparation for Microstructural Characterization

The produced 10x10x15 mm^3 cubic samples were divided along two planes parallel to build direction (BD) and parallel to scan plane (SP), to evaluate porosity, fracture development, and microstructural characteristics. Cross-sectioned, mounted, and polished test specimens were used.

On samples taken from both AB and HT tensile specimens, microstructural investigations were done using OM. Mounting, grinding with abrasive materials up to 2500 grit, polishing with diamond suspension (6 m, 1 m) according to ASTM E3 (“ASTM E3,” 2020) , and etching with 2 percent vol. HNO3 for 30s-60s in ethanol were used to prepare cross-sections for metallographic investigations.

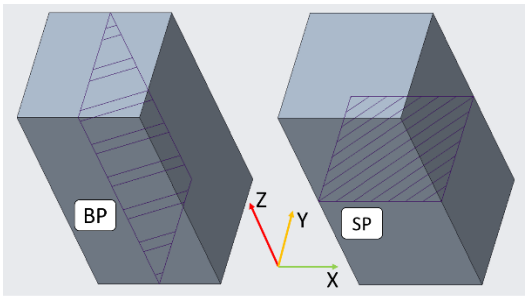

a

Figure 25 LPBF density samples, build plane BP and scan plane SP indication

5.07 Sample Preparation for Magnetic Characterization

To decrease measurement error, the top and bottom surfaces of the ring specimens were milled for surface finish after manufacture. Ring samples with a starting height of 4.5 mm were ground down to a final height of 4.0 mm.

a b

Figure 26 windings on toroid for magnetic characterization; (a) primary winding and (b) secondary winding

The secondary winding of insulated copper wire with N2 = 34 turns was applied

first, with special attention paid to winding the cable as evenly as possible and minimizing the airgap between the wire and the specimen core. On the core, all N2 rounds of wire were wrapped in a single layer. N1 = 34 turns of insulated copper wire were likewise evenly coiled in one layer for the magnetizing winding. Permeameter and equipment used for DC tests, conducted according to the standard IEX 60404-4, are:

1. Keysight 5700 series DC supply (30V, 50A)

2. L.E.E. Digital Fluxmeter

3. supply DC Agilent E3633A

Chapter VI. Results and discussion

6.01 Sample density

Density analysis by gravimetric method shows a decreasing value of porosity increasing volume energy density (VED), calculated as in Equation 2 mentioned before. Being *P* the laser power [W], *v* the scanning speed [mm/s], *t* the layer thickness [mm] and *h* the hatch distance [mm]. VED trend shows, see Figure 27, a typical horizontal asymptote for values greater than 180 J/mm^3 in pure Iron samples, instead for Fe-Si$_3$ was not possible to observe value greater than 200 J/mm^3 due to instability and high-risk failure during the process.

The reason behind such different trend increasing energy input is due to melt pool instability and Silicon vaporization resulting in density value drop [(Spierings *et al.*, 2016; Tan, Wong and Dalgarno, 2017; Muñiz-Lerma *et al.*, 2018; Fang *et al.*, 2020)].

Some samples with low, medium, and high density are shown in Figure 27.

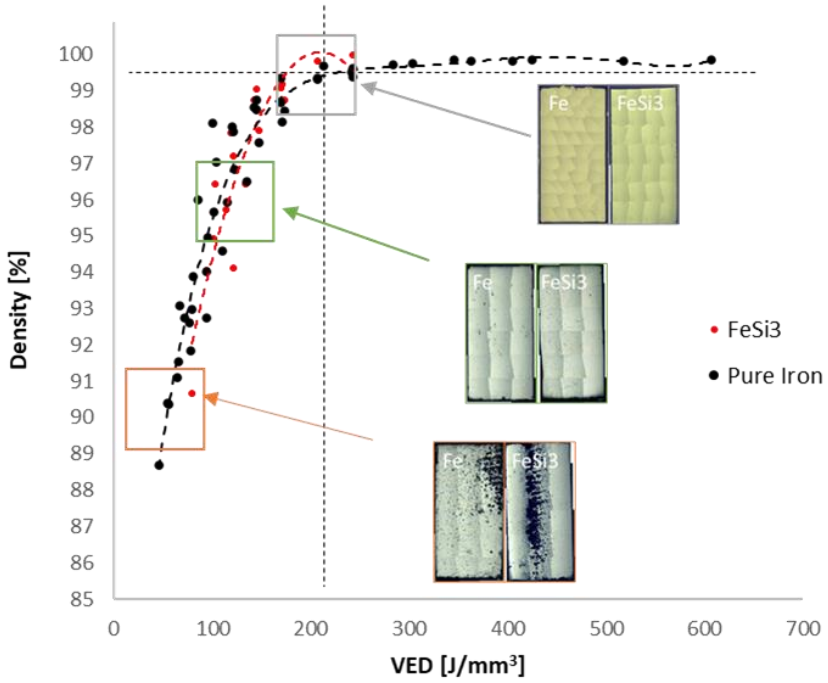

Figure 27 Density variation according to VED for pure Iron and Fe-Si3.

For both materials, full dense specimen was reached with a minimum VED value over to 230 J/mm^3. Optimal set of parameters are shown in Table 6

POWER [W]	Scan Velocity [mm/s]	Hatch Distance [mm]	Layer thickness [mm]
175	500	0.07	0.02

Table 6 Optimal process parameters

6.02 Hardness and microstructure

No micro hardness differences, between bottom and upper zone of the sample, were observed for both powders: in the as build state, pure Iron reached mean values of 200 $HV_{0.2}$ and Fe-Si_3 270 $HV_{0.2}$, in according to the results obtained by other authors were pointed out that they are due to fine microstructure and residual stresses, typical of product fabricated by means of L-PBF.

In bottom figures a microstructure comparison of the AB pure iron (Figure 28) and Fe-Si_3 (Figure 29) is reported. For pure iron were not observed microstructural modification in terms of grain morphology and size, both along build direction and scan direction. Instead for Fe-Si_3 changes in grain orientation occurred on scan and build direction. Along scan plane were not oriented grain beside in build direction plan is possible to observe a preferred orientation.

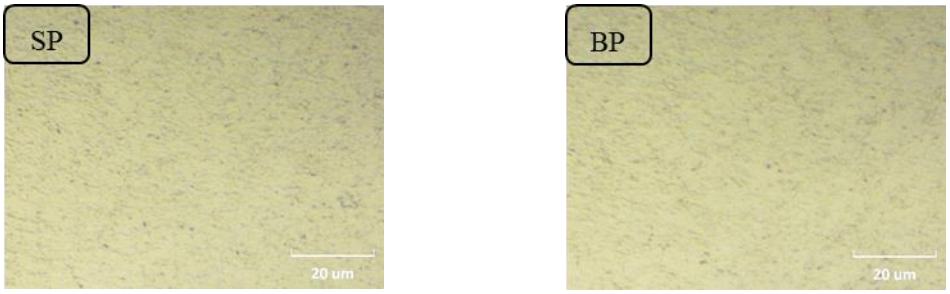

a **b**

Figure 28 Pure Iron etched (3% vol. HNO_3) micrograph, a scan plane (SP) and b built plane (BP)

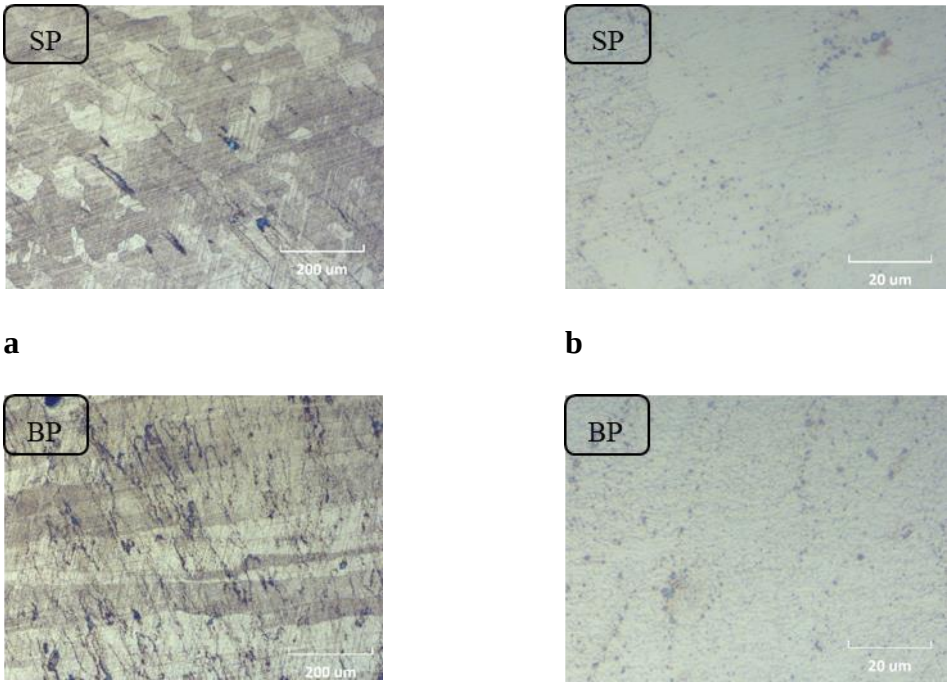

a **b**

c **d**

Figure 29 Fe-Si_3 etched (3% vol. HNO_3) micrograph a and b for scan plane (SP) at different magnification, c and d for built plane (BP) ad different magnification

6.03 Roughness results

Both pure Iron and Silicon Iron samples roughness show decreasing values with VED increasing. Figure 30 shows the roughness results varying VED and scan speed.

A lower roughness can be obtained increasing VED value or decreasing Scan speed rate.

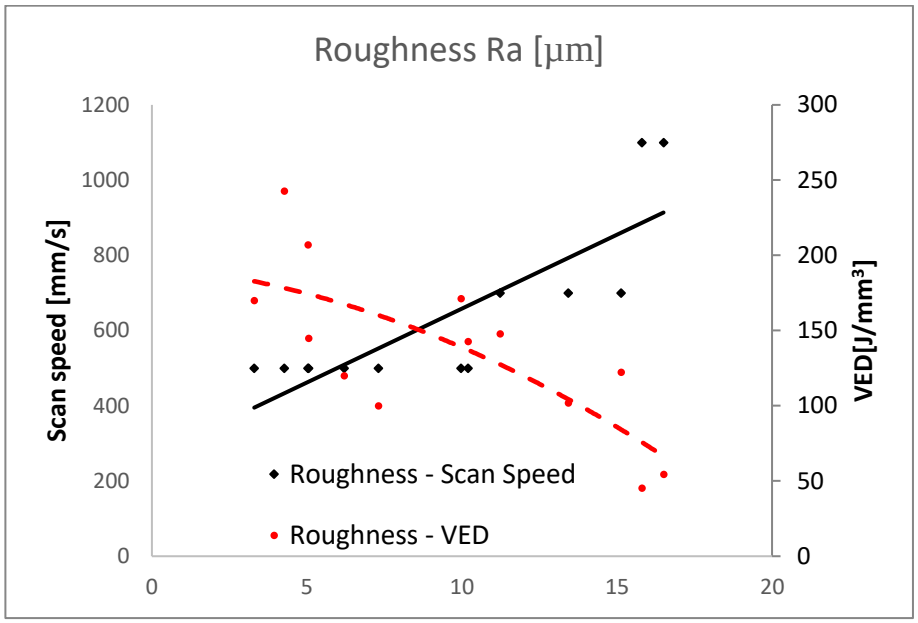

Figure 30 Roughness test results

6.04 Mechanical characterization

Tensile test results are reported in Figure 31 and Table 7Table 7 Tensile tests results.. Pure Iron sample in the as-built state shown a higher ultimate strength value because of L-PBF processes cooling rate. After heat treatment both tensile and ultimate strength exhibit lower value due to microstructure changes and stress relief. As built Fe-Si_3 samples fail at low tensile load due to crystalline plane orientation (*ASM Handbook Vol. 2: Properties and Selection: Nonferrous Alloys and Special Purpose Materials (ASM Int.) 10 Ed., 1990*, 1990; Song, Dong, Deng, *et al.*, 2014; Song, Dong, Liu, *et al.*, 2014; Palousek *et al.*, 2017; Carluccio *et al.*, 2019) and, for this reason, a heat treatment is necessary after L-PBF production. The combination of high stresses and lower mechanical strength on the scan plane led to brittle failure.

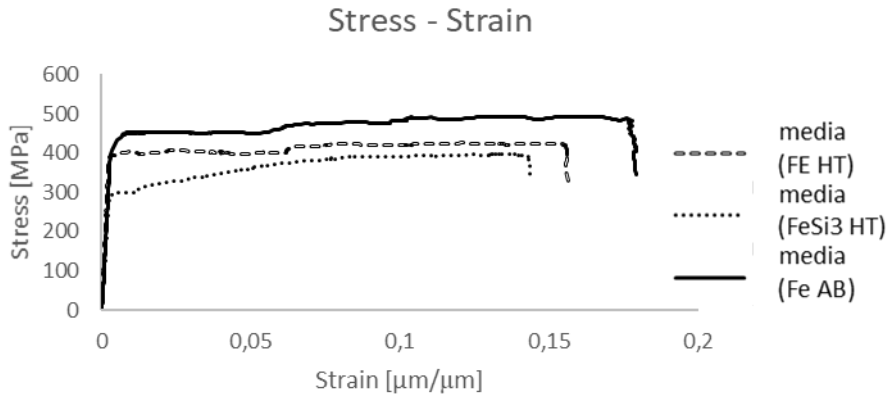

Figure 31 Tensile test results

Sample	E [GPa]	YS [MPa]	UTS [MPa]
Fe AB	164,9	446	491
Fe HT	165	379	407
FeSi3 HT	128	295	425

Table 7 Tensile tests results.

6.05 Magnetic characterization

Direct Current (DC) magnetization was measured for as built and heat treated (850 C° 1h) specimens. For pure iron curve a knee at lower value of magnetic field (*H*) (100 A/m) is noticeable this is related to domains walls displacement. At higher field value, around 1000 A/m it is the only magnetization mechanism (Degauque *et al.*, 1982; "Characterization and measurement of magnetic materials," 2004; "Introduction to magnetic materials," 2009; Ferrara *et al.*, 2015). The magnetization curve of the AB sample appears almost flat, from 0 to 400 A/m, and for a shorter interval the same behavior is visible in HT samples.

AB ring compared to HT one exhibits smaller coercivity (*HC*) and higher magnetic permeability (μ_{max}). In particular, following the annealing treatment HC has decreased by about 30% and μ_{max} has more than doubled. Since, from microstructural analysis, the HT did not induce a noticeable growth of grains, these differences are related to residual stresses relief.

A good level of purity of powder and high density of L-PBF sample is confirmed by a remarkably high value of J ~1.8 T corresponding to ~0.8 JS (de Campos, Teixeira and Landgraf, 2006; Garibaldi *et al.*, 2018; Tiismus *et al.*, 2020).

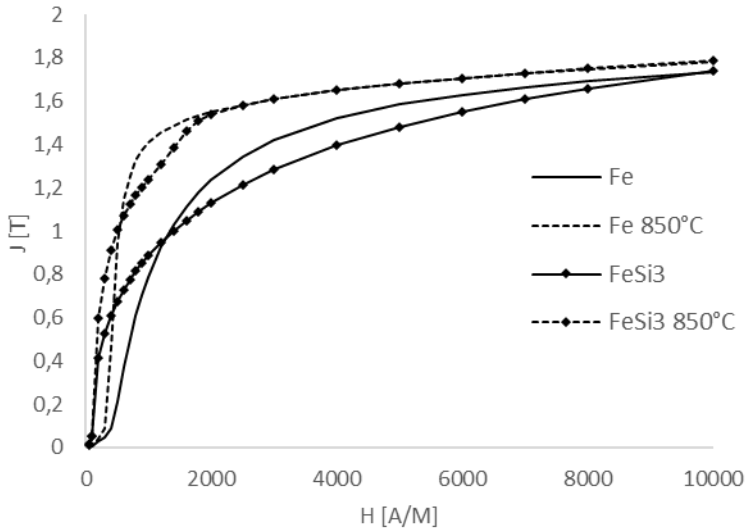

Figure 32 first magnetization curve pure iron and silicon iron

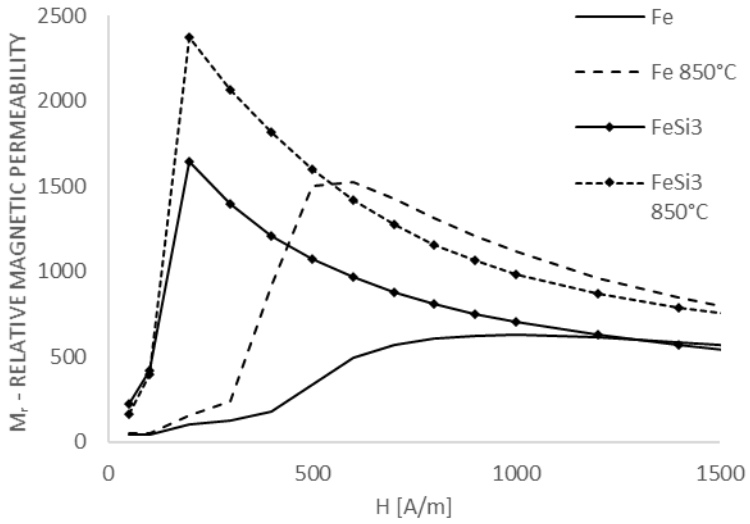

Figure 33 relative magnetic permeability pure iron and silicon iron

Chapter VII. Electrical Machine Design

7.01 Introduction

This chapter initially outlines the Finite Element Analysis-based design workflow, which includes the interconnections between the various software tools used. The electrical machine is described next, followed by the construction of the Finite element model.

7.02 Design Workflow

In collaboration with design department of mechanical engineering and electric engineering a rotor for pure reluctance electric motor was designed as a task to complete the PORfesr project “ACMec”.

The objective of this project was to evaluate the possibility of realizing a pure reluctance rotor geometry with a high number of flux barriers (compared to conventional geometries such as the one in the Figure 34).

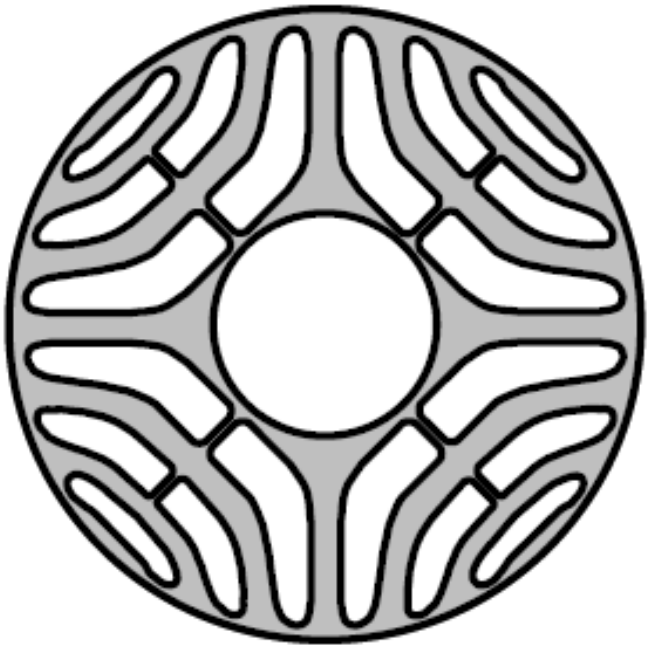

Figure 34 rotor design example

The difficulty in the design of this type of electric motor consists in realizing analytical models that can easily consider the behavior of the motor, and thus be able to study the differences in performance as the degrees of freedom vary in the definition of the geometry. The complexity increases further when the number of flow barriers is increased. For these reasons, the design of pure reluctance motors, and in particular of the rotor under consideration, has been set on the use of numerical software and optimization algorithms. The following are the key points of the methodology used:

1. Stator and winding identification
2. Characterization of magnetic materials for the realization of the rotor
3. Identification of secondary effects since the rotor is not laminated
4. Preliminary studies of the phenomenon
5. Identification and setup of numerical simulation software
6. Choice of optimization methodology (optimization steps, parameters of the optimization algorithm and of the numerical model in the different steps)

(1) Stator and winding identification

For the purposes of this project, the stator of a conventional motor was taken as a reference.

The main parameters of the stator are as follows:

- Number of pole pairs p=2

- Number of slots Ns=24

- Conventional rolled ferro-silicon material

Figure 35 Stator of Syn Rm electrical machine

The main winding parameters are as follows:

- Full pitch and single layer winding (2 slots per pole and per phase)

- Conductors in series per slot n = 20 (obtained by 3 enameled wires in parallel of

bare diameter 0.80 mm, 0.86 mm with enamel, for a total of 30 mm^2 of copper in the slot). Considering the quarry area of about 68 mm^2, the filling factor is 0.44.

- Possibility to connect the coils in series in different ways for better adaptation to the converter (in the final prototype this will not be done)

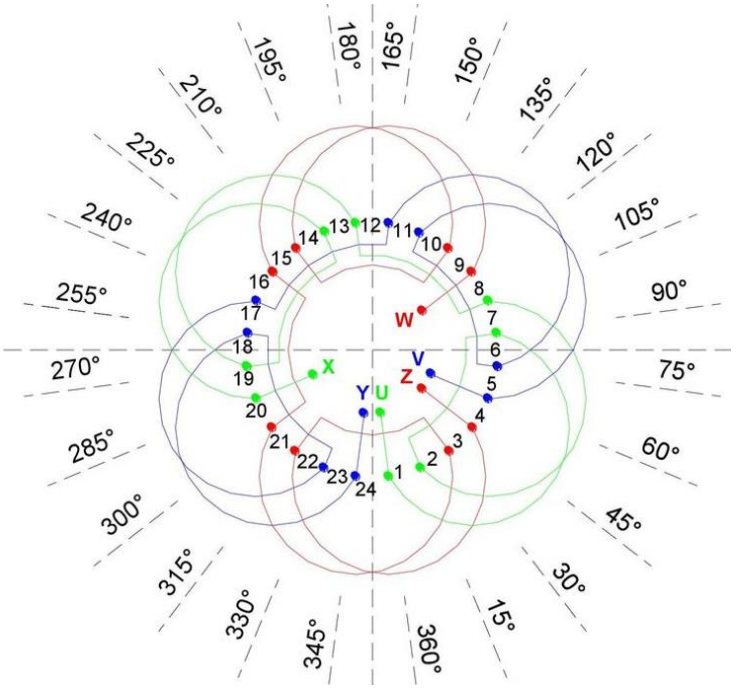

Figure 36 windings detail

(2) Characterization of magnetic materials for the realization of the rotor

In order to design the rotor, it was necessary to magnetically characterize the printed material.

The characterization allowed to define advantages and criticalities of the different materials. In particular, the significant advantage in annealing the materials was highlighted.

Six specimens were fabricated and named as A, B, C, D, E, F.

Label	A	B	C	D	E	F
D ext. [mm]	79.2	79.1	79	80.2	80.2	80.2
D int. [mm]	71.2	71.2	71.5	70	70	70
h [mm]	9.8	9.8	9.8	10	9.9	9.8
t [mm]	4	4	3.8	5.1	5.1	5.1
Material	Fe	Fe	Fe	Fe-3%Si	Fe-3%Si	Fe-3 %Si
Heat Treatment	As Built	700°C 1 h	850°C 1h	As built	700°C 1 h	850°C 1h
Volume [cm^3]	9.260912	9.139071	8.687878	12.03261	11.91229	11.79196

Table 8 Detail of toroids for magnetic characterization

The measurement is carried out using a primary winding (a) and a secondary winding (b, superimposed on the primary winding) as seen in Figure 26

Measurements were conducted according to the standard: ("IEC 60404-4 :Magnetic materials - Part 4: Methods of measurement of d.c. magnetic properties of iron and steel," 2020).

Legend:

B →Magnetic Induction

H →Generated Magnetic Field

Mur →Real magnetic permeability

Hc →Coercive field

Br →Magnetic remanence

Sample Results:

B-H curve:

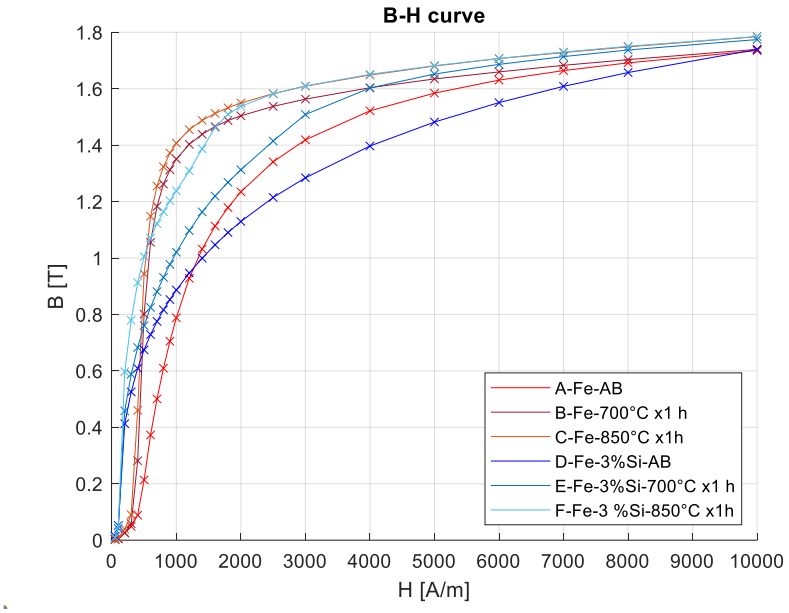

Figure 37 first magnetization curve B-H

B-H curves (copied for symmetry for graphical purposes only) with markers to highlight the values of residual induction *Br* and coercive field *Hc*. It can be seen that annealing led in all cases to a reduction in coercive fields. Therefore, a benefit in terms of lower hysteresis losses is expected. An increase in residual induction is also noted.

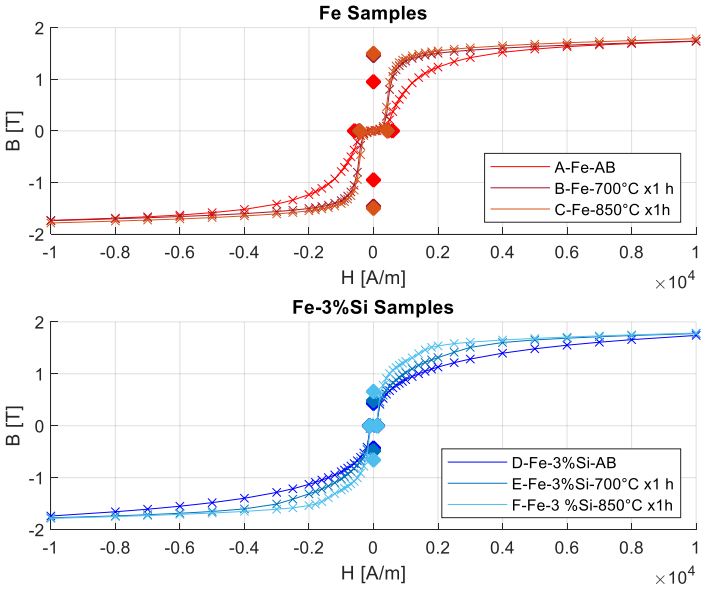

Figure 38 first magnetization curve B-H horizontal symmetry

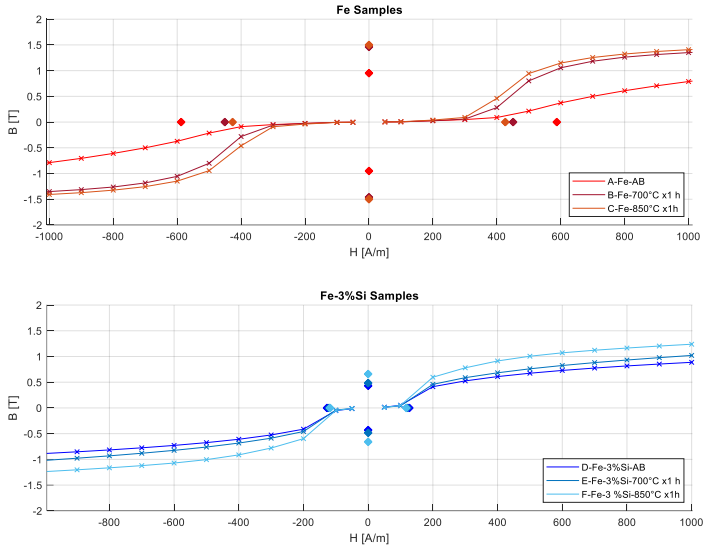

Figure 39 Detail of B-H curve horizontal symmetry

Relative permeability: on all samples, the improvement in relative permeability obtained by annealing the materials is noted.

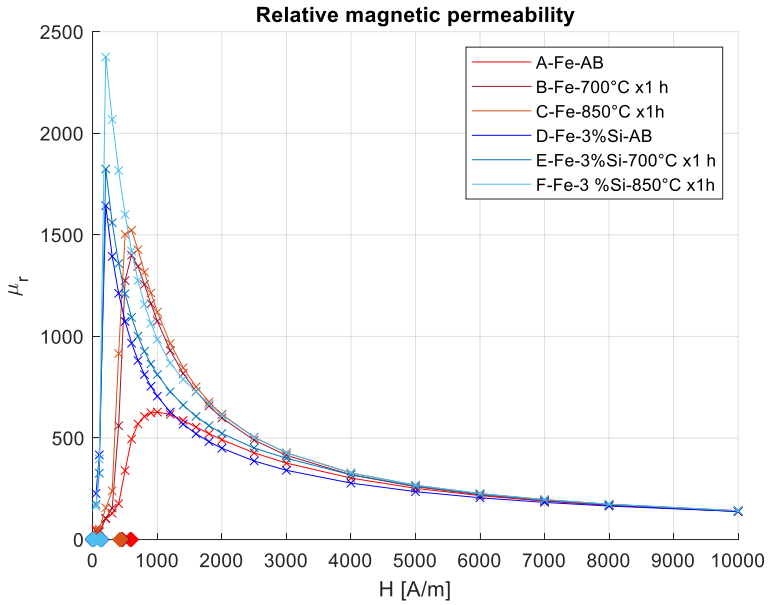

Figure 40 relative magnetic permeability

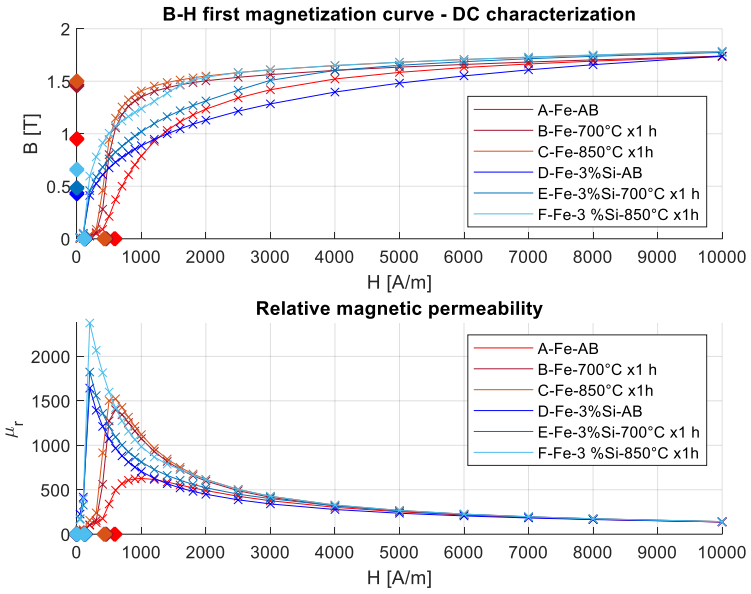

Figure 41 comparison of first magnetization curve and relative magnetic permeability

(3) Identification of secondary effects since the rotor is not laminated

One part of the study involved a qualitative analysis of secondary effects since the rotor is not laminated but solid. These effects were confirmed in the literature and verified by preliminary finite element simulations.

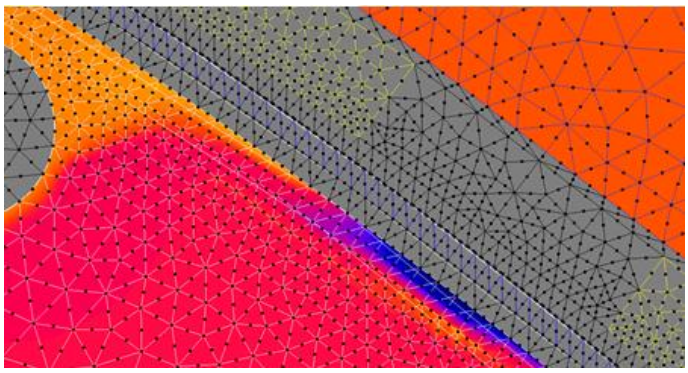

Figure 42 secondary effects detail

Current thickening in thin rotor volumes facing the air zones (barrier-air gap)

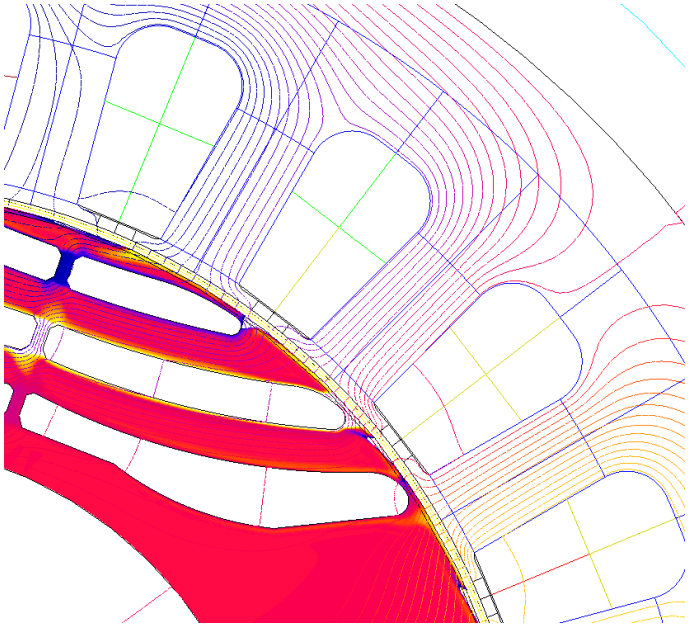

Figure 43 current thickening in thin rotor areas

(4) Preliminary studies of the phenomenon

The main effect due to the non-rolling of the rotor plate is to have induced currents on the rotor iron due to the presence of fluxes flowing through the rotor magnetic circuit that are not synchronous with the rotor itself. These fluxes are due to the distribution of stator currents in the slots (rather than a sinusoidal conductor distribution), the presence of the stator slots themselves, and the particular rotor geometry in which the rotor consists of alternating ferromagnetic flux channels and flux barriers (air channels).

These "eddy" currents result in additional losses on the rotor and effects on torque control dynamics. In particular, the structure would theoretically allow for an asynchronous torque characteristic (the motor is theoretically self-starting, by a principle similar to that of squirrel-cage asynchronous motor operation).

(5) Identification and setup of numerical simulation software

The software selected for the simulations is the open-source software FEMM 4.2: (“FEMM 4.2,” 2020)

This software is widely used in the study and design of electric motors in industry and academia, even for scientific research purposes. The main reason is because the developers have set up and gradually updated the software just for the study of electric motors.

Given the need to perform a significant number of simulations and analysis, it was decided to use an additional open-source software, SyR-e, dedicated to the optimization of electric motors https://sourceforge.net/projects/syr-e/ . This software has been realized thinking about the realization of pure reluctance synchronous motors, in perfect agreement with the request of this project. Graphical interface of SyR-e is shown in Figure 44.

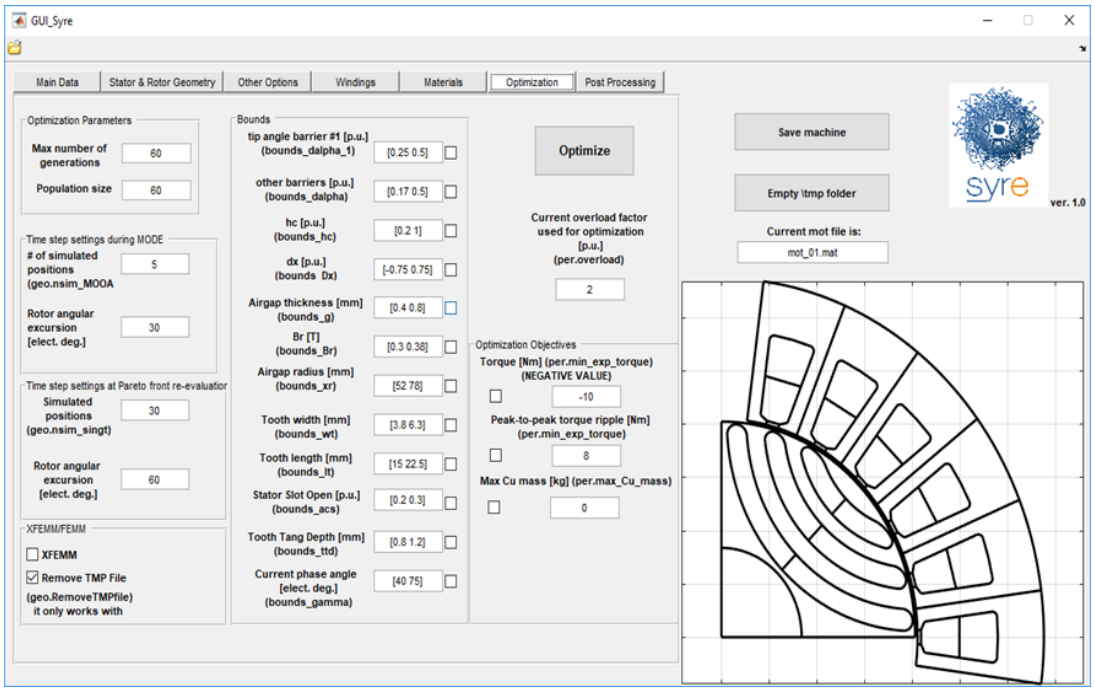

Figure 44 Graphical interface of the SyR-e software is shown below:

The software has been partly modified to meet the needs of the project. First of all, the new magnetic materials have been inserted according to the results obtained from

the magnetic characterizations.

The modifications to the code, made possible thanks to the access by the user to all the low level codes of the program, have mainly concerned the elimination of automatisms which increased the computational time of the optimizations.

(6) Choice of optimization methodology

The optimization was carried out in several phases, gradually moving towards more in detail: Optimization steps, parameters of the optimization algorithm, and of the numerical model in the different steps.

The first optimizations were used to define a parameter racket that maximizes the average torque. Subsequently, the optimizations were increasingly oriented towards minimizing the torque oscillation (ripple). Consequently, the parameters that have a significant effect on the average torque have been kept as constant as possible while those associated with torque ripple have been varied.

By way of example, the parameter that most influences the average torque is the rotor air-iron ratio (in the following picture it depends on the choice of Lfe and Lair). The parameters that have the greatest effect on torque ripple are associated with the number of barriers and their relative shape and position (the figure shows the angles that determine the relative position between flow barriers) (Bianchi, Degano and Fornasiero, 2015).

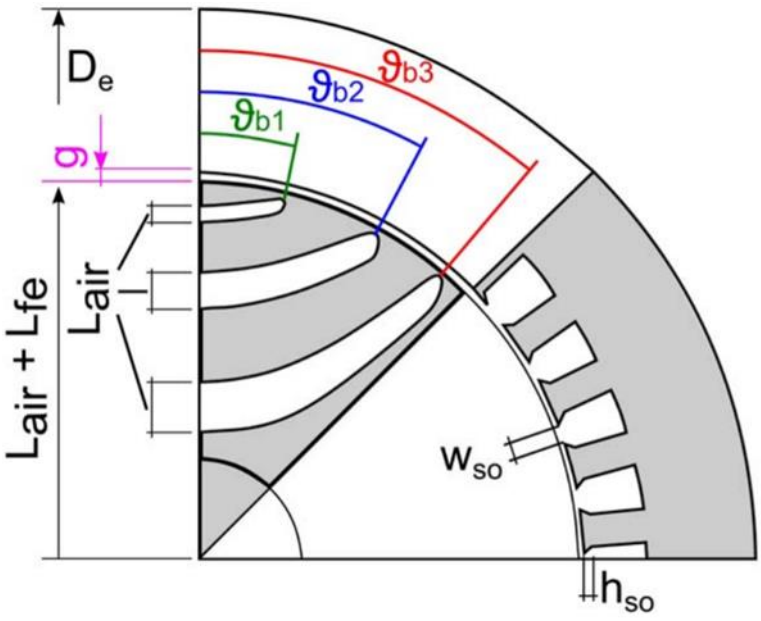

Figure 45 parameters effecting torque ripple, from (Bianchi, Degano and Fornasiero, 2015)

Once the design/optimization method was identified, it was essential to identify in the different steps the level of accuracy suitable for the simulations that are implemented at each iteration of the optimization algorithm. They are evidenced between these:

- the simulation step (how many rotor positions are simulated for each individual)

- the mesh (grate that determines the number of regions in which the physical dominion it comes discretization in order to be able to implement simple differential equations to the aim to resolve the complicated physical problem of the complete dominion).

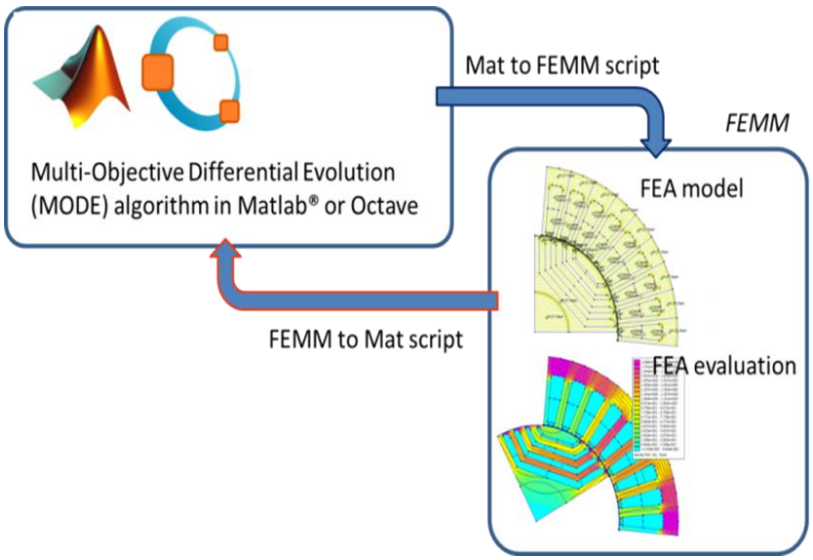

Figure 46 workflow scheme

7.03 Optimization Algorithm:

Optimization was carried out using a MOOA (Multi-Objective Organic Algorithm) type algorithm More specifically, a MODE (Multi-Objective Differential Evolution) algorithm was used.

Having chosen the number of generations and the population size, the algorithm is based on three main steps:

- Mutation;

- Crossover;

- Selection.

During the mutation phase, from each generation are selected in a pseudo-random way three distinct individuals: xr, xs and xt, whose combination, through the use of a weight function F, allows to obtain an individual called xoff. Such individual can be obtained in the following way:

$$x_{off} = x_S + F(x_r - x_t)$$

The function F has a range from variation between 0 and 1. F then controls the magnitude of the exploration vector (xr -xt) and this determines how far from the point xt xoff must be generated. The different versions are distinguished from each other by a different mutation function (Storn and Price, 1997).

Obtained the mutated vector xoff, an operation defined crossing is carried out between it and the target individual, defined previously. The crossover operation thus allows to obtain a greater diversity of individuals. The combination between the two individuals allows to obtain a new individual called test individual. The functioning of this procedure can be seen from the following figure:

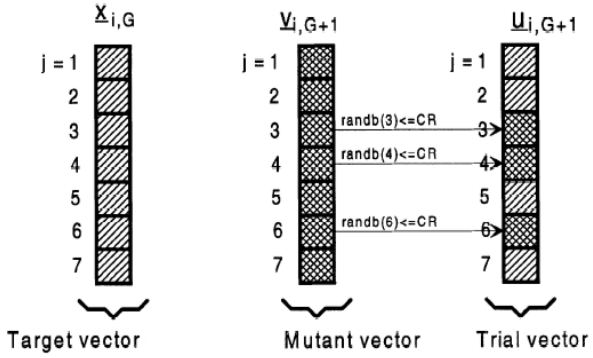

Figure 47 Graphical explanation of how the crossover operation works

We note the presence of the constant CR, which is included between 0 and 1. Also the function randb(j) is included between 0 and 1. When it is verified that the random function is less or equal CR, the value of the mutated vector is saved in the test individual, otherwise the element of the target individual is taken. The test individual cannot be equal to the target individual, so at least one parameter of the mutated individual must be present in the test individual.

The last phase is the selection phase. To decide which individual will be part of the next generation we compare the test individual and the target individual. In this case we want to evaluate which of the two leads to a smaller cost function, so if the test individual leads to a smaller cost function, it becomes the new target individual, otherwise the target individual is not changed.

The output of the software at the end of each optimization is a set of graphs and tables showing the performance of the best motors that have been obtained (it is possible later to simulate in more detail the performance of the optimal motors). An example of these outputs is shown below (note that due to the type of settings used in this particular case, the software output torque ripple values multiplied by 10).

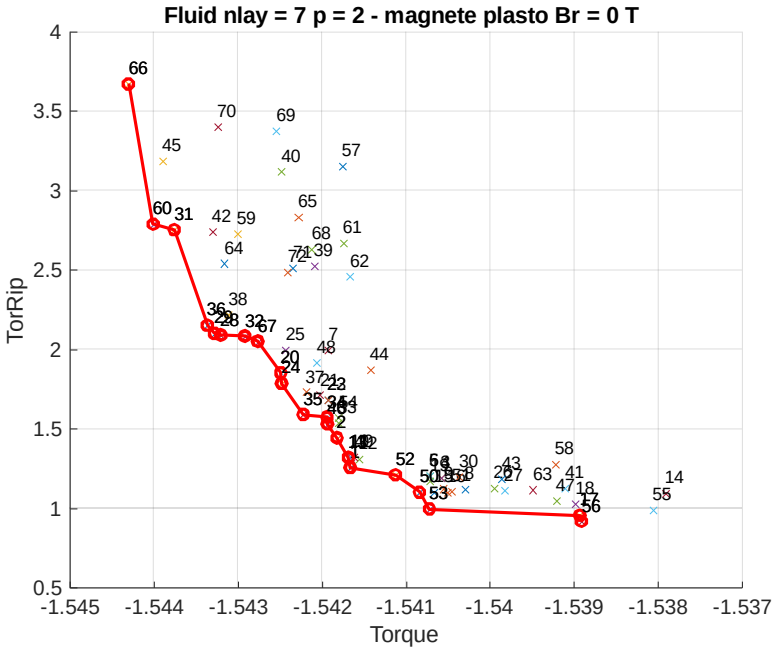

Figure 48 results of optimization

7.04 Geometrical optimization results

Geometric constraints imposed during the definition of the geometry led to the selection of a number of 7 flow barriers as a compromise value.

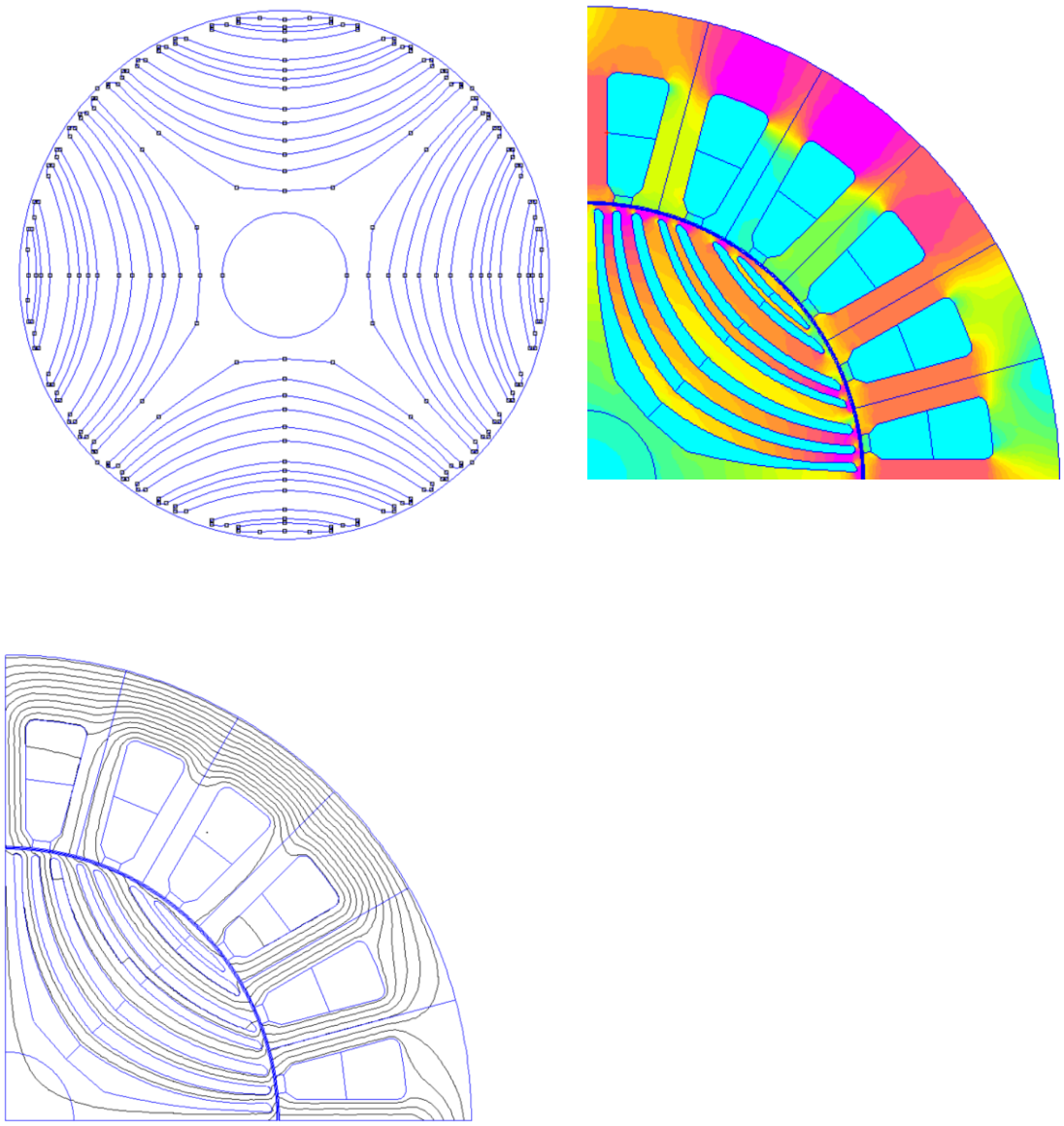

Figure 49 Geometrical representation of core design and results of FEM simulation

Since the application does not involve high rotational speeds, the motor was sized

without internal jumpers (which are typically present to improve the mechanical performance of the rotor structure).

If it were necessary to introduce such jumpers, the suggested procedure for strengthening the mechanical structure would have been topological optimization. Examples of the results of such optimization were tried on a conventional rotor and are given below (from left to right the results for increasing maximum speeds). The procedure can be repeated similarly for structures with more barriers.

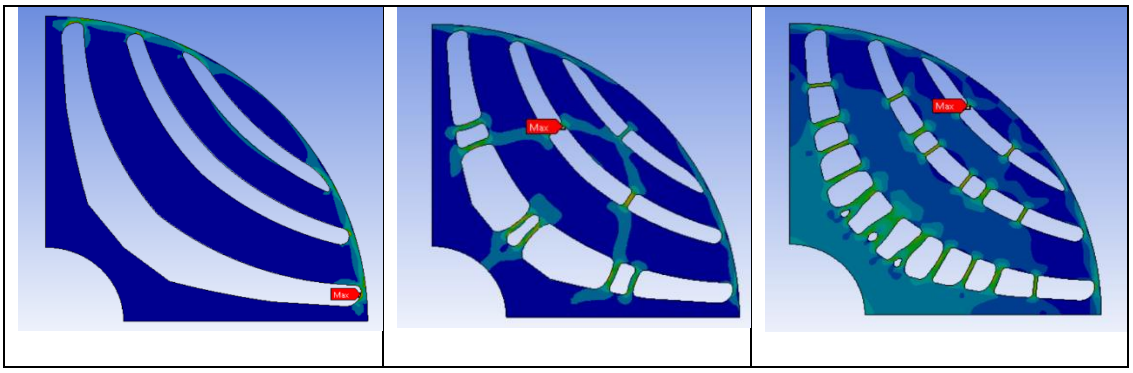

Figure 50 Mechanical design optimization examples

Since the application does not involve high rotational speeds, the motor was sized without internal jumpers (which are typically present to improve the mechanical performance of the rotor structure).

The effect of adding such jumpers on the torque and its oscillations must then be validated by electromagnetic simulations.

Optimization of torque performance:

Optimization was done to achieve an average torque around 1.5 Nm while trying to minimize its oscillations.

The geometric parameters that were made to vary are:

- Position of the flow barriers, the range of variation of the first and subsequent barriers;

- Thickness of the flow barriers, also considering the minimum tolerance of the

achievable thickness;

- Displacement "Δx" of the flow barriers with respect to the point in which the barrier ends when approaching the machine air gap;

The parameters of each simulation carried out are:

- Rotor rotation angle to be analyzed in electrical degrees;

- Number of angular positions in which the angle to be analyzed is divided;

- Density of the mesh used

The parameters of the optimization that were modified during the different phases are:

- Number of generations

- Population size of each generation

Added to these is the optimal current angle (the one that provides the highest average torque), which was used as an optimization variable in the early stages of the overall optimization.

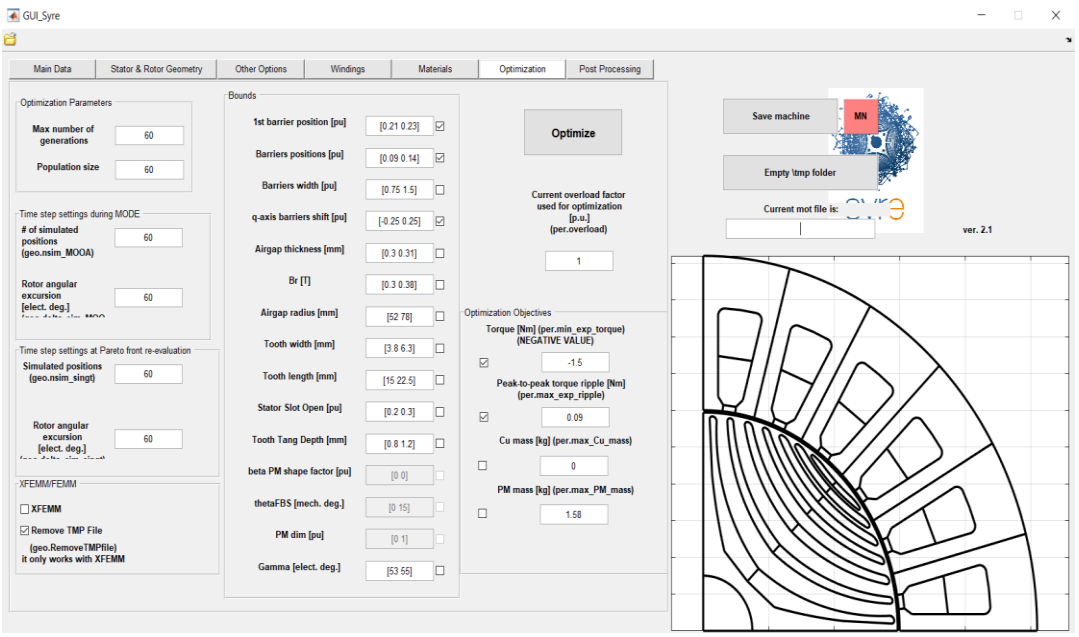

Figure 51 Overview of parameters used for simulation

The final outcome obtained are resulted in the following:

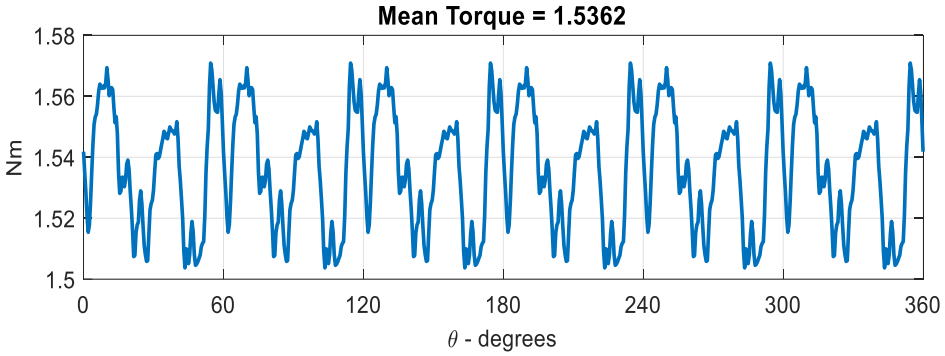

Figure 52 torque ripple graph

That is, an average torque of 1.54 Nm with an oscillation of about 0.067Nm peak-to-peak, equivalent to about 4.4% of the average torque [(1.57085-1.50375)/1.5362=0.044].

The high number of flow barriers generates a torque profile with content even at quite high frequencies compared to what would be expected from a conventional motor. For this reason, the final rotor optimizations were performed with very small rotor rotation steps (60 steps in 60 electrical degrees), a high number of generations and individuals per population (60 and 120) and a dense mesh.

7.05 Mechanical simulation

A numerical simulation for mechanical stresses were done considering 600, 1200 and 3000 rpm, for simplicity a quarter of rotor is considered and a total force (Fc) equal to centrifugal force is applied in center of mass for bridges, see Figure 53.

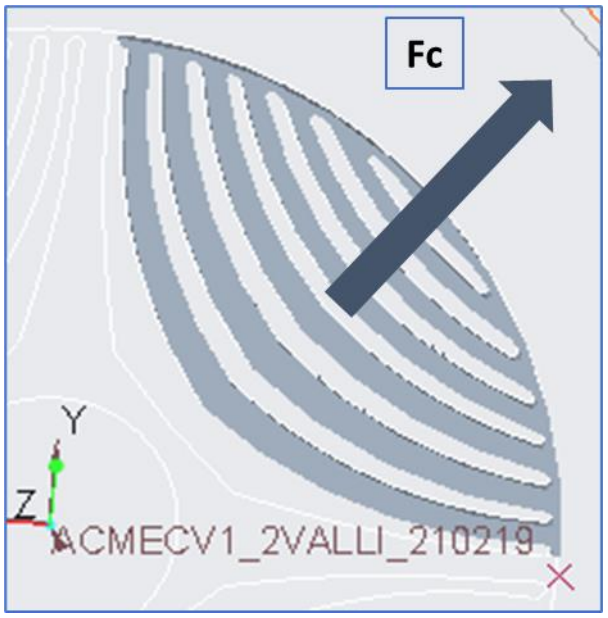

Figure 53 schematics of forces and volume considered

As input data:

Density	7.83E+03	kg/m^3
Inertia	2.84E-04	kg*m^2
Radius	2.97E-02	m
Mass	6.04E-01	kg

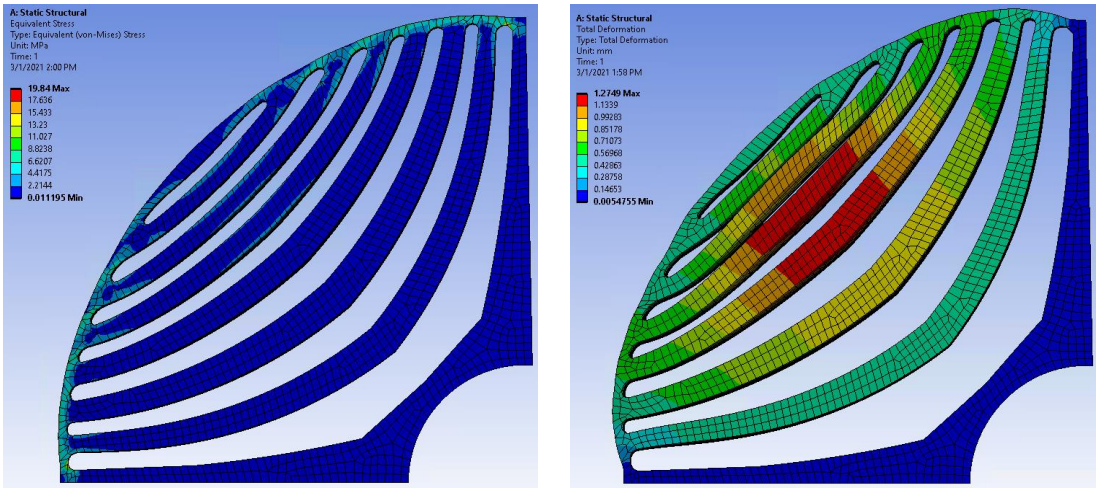

a b

Figure 54 FEM results for centrifugal force: equivalent stress using Von Mises (a) and total deformation (b)

Max Cumulative Electromagnetic force:

280 N

Max Cumulative Centrifugal Force @3000rpm

237 N

Max stress and deformation @3000rpm

20 Mpa

1.3 mm

7.06 Rotor Manufacturing

(1) Process Parameter Optimisation

In order to achieve high part quality for a wide range of real-world components, a systematic approach to process parameter optimization should be envisaged. A preliminary attempt to optimize the LPBF process parameters for large component production has been carried out in this research using the same LPBF machine used for initial tests, the Sisma Mysint 100 RM.

All the samples were built with 3 mm high conic support structure to facilitate removing stage without damage to the samples. The first attempt with same process parameters used to maximize density shown an higher thermal stress gradient at the end of support structure and starting of part, warping the initial part layer (Figure 55).

Figure 55 Defective first layer

The aim is to solve this problem, very common during the transition from simple geometry samples production to real part manufacturing, due to high thermal gradient. It's important to find a solution without decreasing input VED and so avoiding decreasing on density value. The solution was to increase the of rotor height by 1mm and remove all support structure from the slicing software, a perfect contact with platform is granted, lowering overheating and thermal gradient. Using this solution makes difficult the removal stage so will be necessary a wire electrical discharge machining to avoid too much removed material from final part. Another

solution to reduce residual stresses is a chessboard scan strategy, for this reason, used from the beginning of tests also for density and tensile test specimens. A preliminary prototype was produced as seen in Figure 56-a and a shape accuracy analysis was done using a Zeiss stereo microscope the results are shown in Figure 56-b.

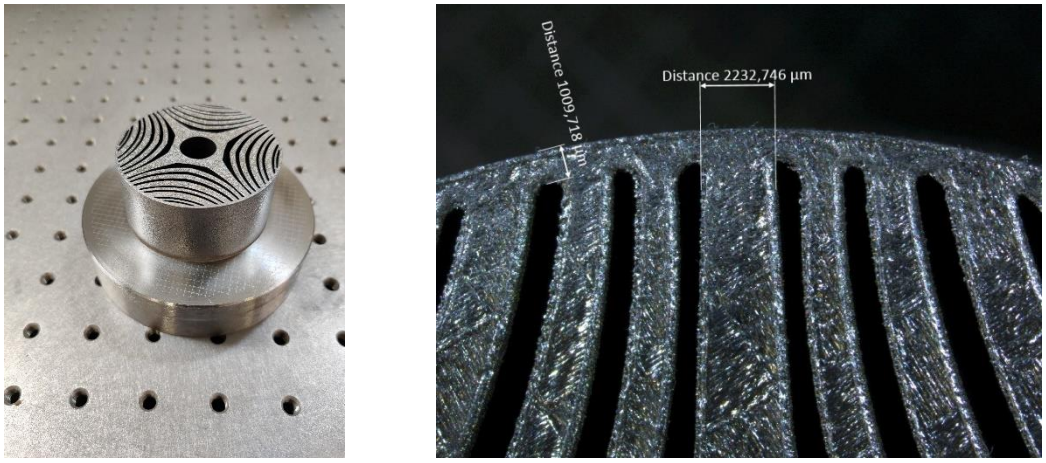

a b

Figure 56 Prototype realization (a) and dimensional accuracy analysis (b)

Comparing the results to the original cad data, a difference below 0.05 mm was measured. Considering this results it was not necessary to modify shrinkage value on slicing software so the final rotor was printed using the same process parameter of prototype.

Figure 57 Final SYN RM rotor

A total printing time of 44h is needed to complete building of rotor core, not including powder heat treatment, sewing of needed amount of powder and loading in LPBF machine before printing, unload of finished print job and de-powdering.

(2) Rotor post processing

To be able to manipulate a complex part like the rotor, it is necessary a deep de-powder stage to avoid contamination in successive processes. Once mostly of unprocessed powder particles were removed a cleaning with alcohol was used to prevent flying powder and, to prevent oxidation, a full cover with mineral oil.

With rotor cleaned and protected from rust, it is possible to cut it from steel baseplate, before proceeding with this process a heat treatment in inert atmosphere furnace was done as described in Figure 58 granting a reduction of residual stresses and rising magnetic properties.

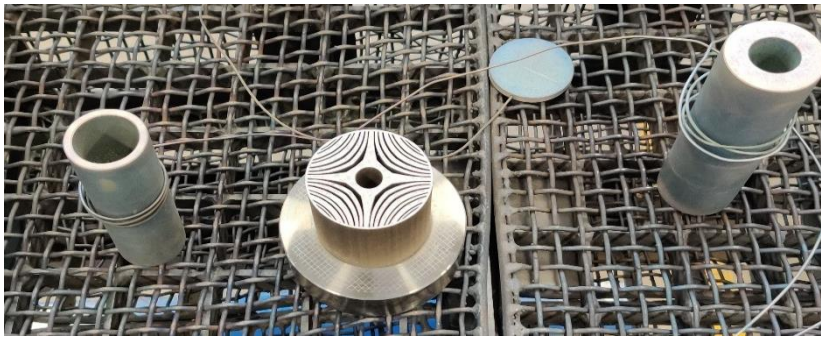

a

b

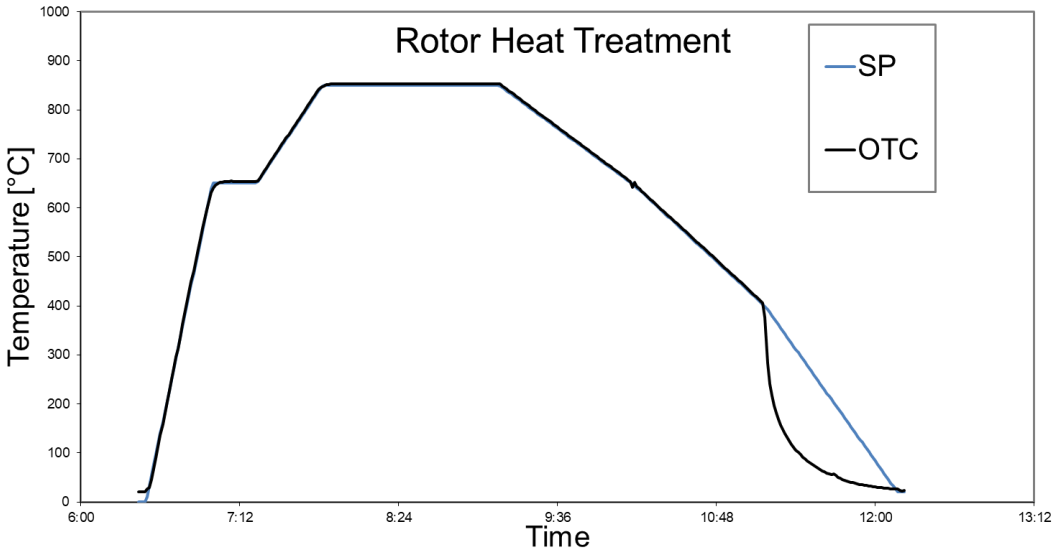

c

Figure 58 Rotor heat treatment: a loading into furnace with two other sample for comparison, b furnace, c thermal cycle (SP set point, OTC sample thermo couple)

Once heat treatment done, some post processes like turning and grinding are needed to obtain required precision and surface roughness. 5 mm of allowance were added on top surface to be sure to have enough material to remove during milling process. Once planar surfaces machining was done is necessary grant a perfect coaxially from rotation axe and rotor symmetry axe, for this reason a drilling and final boring on central hole were done to grant a correct mounting on shaft, from 13.4mm to 14mm (Figure 59).

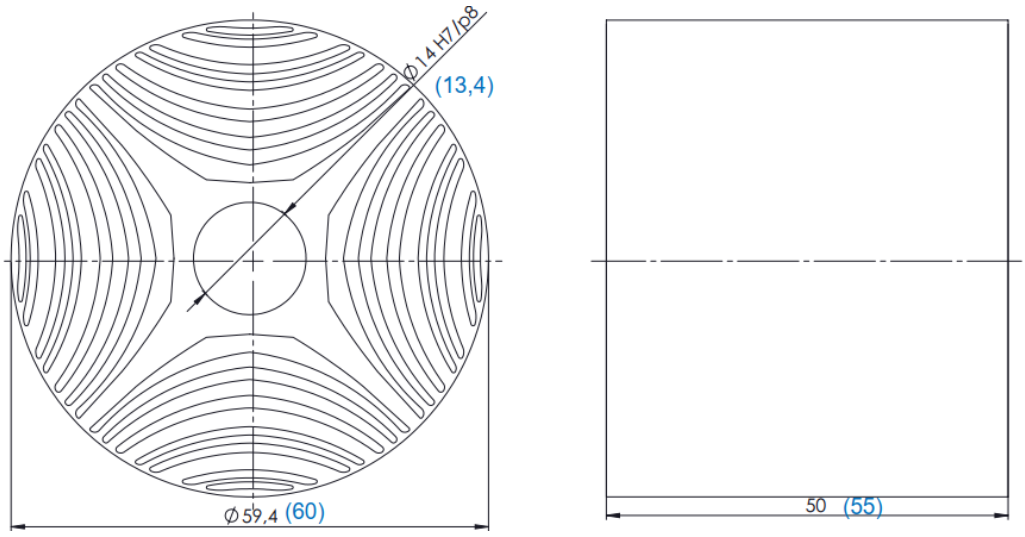

Figure 59 rotor design with material allowance for post processing phase (measurements in brackets)

A total printing time of 44h is needed to complete rotor building, almost 1h for wire electron discharge machining and 7h for heat treatment.

The shaft and the rotor will be mounted by interference using a hydraulic press, once the two parts are jointed together, a turning on external cylindrical surface is needed to grant a correct gap between stator and rotor, maximizing the performances by minimizing air gap, starting from 60mm to 59.4mm

For a correct working of EM, the housing with stator and rotor must be designed in a certain way, an external company is doing the design stage of all parts considering, both, final drawings of shaft for bearing mounts (Figure 60) and air gap between rotor and stator.

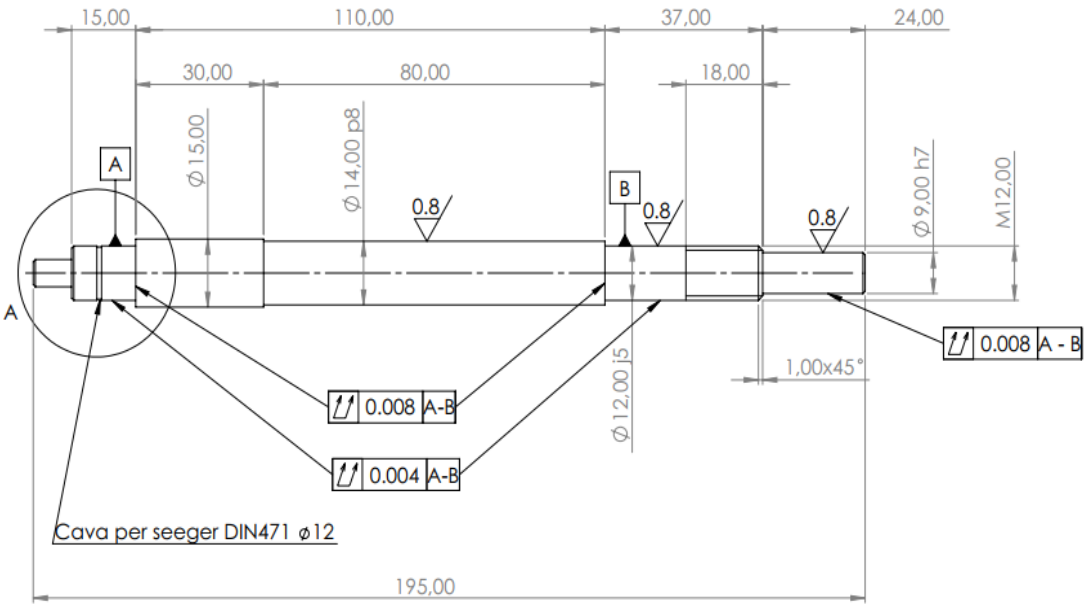

Figure 60 shaft design

The findings indicate that more work could be done to create a full electric motor using LPBF technology. The following are some likely outcomes advancements that could be investigated further:

- Materials: the development of all the parts that make up an electric motor is to be investigated, this involves the study of other materials suitable for the realization of rotor, stator, windings and housing by using LPBF. For the rotor further studies can be done on soft magnetic materials; for the stator part, according to the type of electric machine, it will be necessary to study conductive materials or iron magnetic materials; for the windings it will be of sure future interest to investigate the possibility to process through LPBF materials such as pure copper or its alloys.
- Design: for all materials and parts mentioned above, it will be necessary to study a design that takes into account the LPBF manufacturing technology and the intrinsic properties of the materials processed through it. a thorough magnetic characterization for the ferro magnetic materials combined with a mechanical characterization in the as built and thermally treated state will serve as input data for the correct design; in turn a correct electrical and thermal characterization will

serve as input data for the design of the stator windings.

- Process: the materials mentioned above should also be studied considering the LPBF manufacturing process. Since these materials are difficult to process, a correct choice of the process parameters is as fundamental as the study of the interaction between laser and raw material.

Chapter VIII. General Discussion

The research work carried out has shown, through the results revealed above, a twofold innovation. First, it was possible to produce through the LPBF process ferromagnetic materials suitable for applications in E-mobility. Secondly, it was also possible to design, using finite element software, the rotor of an electric Syn RM motor, optimizing the geometry to reduce weight and torque fluctuations.

As illustrated in Chapter 5.01, using the LPBF technique, fully dense parts can be produced with pure iron and silicon iron, with extremely small round defects within.

Because of the peculiar microstructure provided by the LPBF process, the mechanical properties of the samples are suitable for a functional application, even better than commercial ones, as illustrated in Chapters 5.02 to 5.04.

As aforementioned, the characteristic microstructure of LPBF samples is optimal for high tensile strength, despite magnetic properties, as shown in Chapter 5.05. As a result, a proper heat treatment is required to improve magnetic properties, granting performances comparable to commercial materials currently used.

The achieved results allowed the research project to reach its target of evaluating the potential of LPBF technology in the field of E-mobility, specifically in the area of electric motors and then in particular in a Syn RM rotor core.

This manufacturing process can be used in all aspects, speeding up the stages of design research and prototyping for the traction portion, the connections between the motor and the batteries, and the cooling of all organs engaged in the energy transformation.

8.01 Conclusions and Further Work

(1) Conclusions

A full dense specimen was successfully obtained from both, pure Iron and Iron Silicon 3%, powder through LPBF processes after optimization of process parameters.

The microstructure, mechanical, and magnetic properties of LPBF samples were studied both as-built and after a stress-relief treatment in order to determine their suitability for soft magnetic applications.

The samples were subsequently fabricated and evaluated in both as built and heat-treated conditions for microstructural, mechanical, and magnetic characterizations.

Pure Iron's as-built microstructure was made up of small, non-oriented grains with no indication of melt pool or scan track boundaries, big columnar grains, or solidification sub-structure, with no noticeable change between vertical and horizontal sections. Backward $FeSi_3$ reveals a grain evolution parallel to the scan plane with columnar grains. At high magnification, a dense dispersion of sub-micron, spherical particles were detected.

The magnetic investigation validated the LPBF samples' excellent purity and density, resulting in a magnetic polarization value comparable to commercial ones.

However, because of the fine grain size, DC tests revealed a low magnetic softness, due to the reduction of residual stresses and dislocation density, the stress relief treatment improved the maximum permeability μ_{max} and decreased the coercivity *Hc*, but the measured values are one order worst if compared to literature ones for soft magnetic materials.

In the as-built condition, both SMM's had high hardness and tensile strength, which was attributable to the fine microstructure and high density of dislocations caused by the LPBF process. The stress relief treatment caused a decrease on hardness and tensile strength, as well as increase in ductility. Because of no microstructural changes were seen, these fluctuations were ascribed to a decrease in dislocation density.

To achieve adequate magnetic softness, large grain size is desired, which can be achieved by a high-temperature annealing process, despite mechanical strength.

(2) Further Work

(a) Material

To solve the issue of pure iron and silicon iron alloy processability using LPBF technology, a variety of specific efforts are recommended, including:

- Considering that high Si content is the primary cause of alloy embrittlement, it seems logical that the initial step should be to reduce Si content gradually. Change the alloy's composition to increase ductility and, as a result, reduce the alloy's susceptibility to break when subjected to residual stress. Adding other elements like Cobalt or Nickel to investigate processability. Another element that improves the ductility of the alloy that might be introduced as an alternative to reducing the silicon concentration is Al, which is frequently added to electrical steel to enhance ductility, making laminated and powder core manufacturing less prone to failure. Furthermore, Al raises the resistivity of the material but reduces permeability and saturation polarization.

- Concerning design, a deep modification on shape can be done considering the limit of processability with the LPBF system.

(b) Design

The suggested FEM-based rotor design technique has only been evaluated on one case study, which involves one of the most basic forms of rotor cores. Extending the discovered design technique to different electric motor designs is a natural

progression of this study. Furthermore, it's unclear if the proposed method can be applied to other rotor topologies, particularly the SyR Rm machine.

Specific considerations can be made for electric machines in order to improve productivity and performance. The rotation of the rotor sections, known as skewing, is a classic example of reducing torque ripple (Bomela and Kamper, 2002). Skewing involves complexities at the manufacturing level compared to the traditional construction of stacked laminations. In the case of LPBF type manufacturing technology, this solution is perfectly applicable without any additional complexity.

"Airbus - https://www.airbus.com" (2020).

ASM Handbook Vol. 2: Properties and Selection: Nonferrous Alloys and Special Purpose Materials (ASM Int.) 10 Ed., 1990 (1990).

ASTM (2005) "A341 Standard Test Method for Direct Current Magnetic Properties of Materials Using D-C Permeameters and the Ballistic Test Methods," *Annual Book of ASTM Standards*, i(Reapproved 2011), pp. 1–13. doi:10.1520/A0341.

"ASTM B962 " (2020).

"ASTM E3" (2020).

Bianchi, N., Degano, M. and Fornasiero, E. (2015) "Sensitivity analysis of torque ripple reduction of synchronous reluctance and interior PM motors," *IEEE Transactions on Industry Applications*, 51(1). doi:10.1109/TIA.2014.2327143.

Bomela, X.B. and Kamper, M.J. (2002) "Effect of stator chording and rotor skewing on performance of reluctance synchronous machine," in *IEEE Transactions on Industry Applications*. doi:10.1109/28.980362.

"Bugatti - https://www.bugatti.com/" (2020).

de Campos, M.F., Teixeira, J.C. and Landgraf, F.J.G. (2006) "The optimum grain size for minimizing energy losses in iron," *Journal of Magnetism and Magnetic Materials*, 301(1). doi:10.1016/j.jmmm.2005.06.014.

Cao, W. *et al.* (2012) "Overview of electric motor technologies used for more electric aircraft (MEA)," *IEEE Transactions on Industrial Electronics*, 59(9).

View publication stats

doi:10.1109/TIE.2011.2165453.

Carluccio, D. *et al.* (2019) “Comparative Study of Pure Iron Manufactured by Selective Laser Melting, Laser Metal Deposition, and Casting Processes,” *Advanced Engineering Materials*, 1900049, pp. 1–9. doi:10.1002/adem.201900049.

Catchpole-Smith, S. *et al.* (2017) “Fractal scan strategies for selective laser melting of ‘unweldable’ nickel superalloys,” *Additive Manufacturing*, 15. doi:10.1016/j.addma.2017.02.002.

“Characterization and measurement of magnetic materials” (2004) *Materials Today*, 7(11). doi:10.1016/s1369-7021(04)00512-7.

Chukwuchekwa, N. (2011) “Investigation of magnetic properties and Barkhausen noise of electrical steel,” *#PhD Thesis* [Preprint], (December). Available at: http://orca.cf.ac.uk/24172/.

David, S.A., Babu, S.S. and Vitek, J.M. (2003) “Welding: Solidification and microstructure,” *JOM*, 55(6). doi:10.1007/s11837-003-0134-7.

Degauque, J. *et al.* (1982) “Influence of the grain size on the magnetic and magnetomechanical properties of high-purity iron,” *Journal of Magnetism and Magnetic Materials*, 26(1–3). doi:10.1016/0304-8853(82)90166-4.

“EOS Gmbh - https://www.eos.info/en” (2020).

Fang, Z.C. *et al.* (2020) “Review on residual stress in selective laser melting additive manufacturing of alloy parts,” *Optics and Laser Technology*. doi:10.1016/j.optlastec.2020.106283.

View publication stats

"FEMM 4.2" (2020). Available at: https://www.femm.info/wiki/HomePage (Accessed: October 26, 2021).

Ferrara, E. *et al.* (2015) "Microstructure and magnetic properties of pure iron for cyclotron electromagnets," *Journal of Alloys and Compounds*, 615(S1). doi:10.1016/j.jallcom.2014.01.217.

Finken, T., Felden, M. and Hameyer, K. (2008) "Comparison and design of different electrical machine types regarding their applicability in hybrid electrical vehicles," in *Proceedings of the 2008 International Conference on Electrical Machines, ICEM'08*. doi:10.1109/ICELMACH.2008.4800044.

Fiorillo, F. *et al.* (2016) "Soft Magnetic Materials," *Wiley Encyclopedia of Electrical and Electronics Engineering* [Preprint]. doi:10.1002/047134608X.W4504.pub2.

Fujieda, T. *et al.* (2017) "Kou S (1987) Welding metallurgy, New York," *Materials Science and Engineering: A*, 21(1).

Galea, M. *et al.* (2014) "Development of an aircraft wheel actuator for green taxiing," in *Proceedings - 2014 International Conference on Electrical Machines, ICEM 2014*. doi:10.1109/ICELMACH.2014.6960537.

Garibaldi, M. *et al.* (2018) "Effect of annealing on the microstructure and magnetic properties of soft magnetic Fe-Si produced via laser additive manufacturing," *Scripta Materialia*, 142, pp. 121–125. doi:10.1016/j.scriptamat.2017.08.042.

Garibaldi, M., Gerada, M. and Hague, R. (2018) "Laser Additive Manufacturing of Soft Magnetic Cores for Rotating Electrical Machinery : Materials Development and Part Design," (December 2018).

View publication stats

"IEC 60404-4 :Magnetic materials - Part 4: Methods of measurement of d.c. magnetic properties of iron and steel" (2020).

"Introduction to magnetic materials" (2009) *Materials Today*, 12(3). doi:10.1016/s1369-7021(09)70091-4.

"ISO 6892-1" (2020).

"ISO6507 " (2020).

Jhabvala, J. *et al.* (2010) "On the effect of scanning strategies in the selective laser melting process," *Virtual and Physical Prototyping*, 5(2). doi:10.1080/17452751003688368.

Kim, S.C. (2013) "Thermal performance of motor and inverter in an integrated starter generator system for a hybrid electric vehicle," *Energies*, 6(11). doi:10.3390/en6116102.

King, W.E. *et al.* (2014) "Observation of keyhole-mode laser melting in laser powder-bed fusion additive manufacturing," *Journal of Materials Processing Technology*, 214(12). doi:10.1016/j.jmatprotec.2014.06.005.

Koseski, R.P. *et al.* (2005) "Microstructural evolution of injection molded gas- and water-atomized 316L stainless steel powder during sintering," *Materials Science and Engineering A*, 390(1–2), pp. 171–177. doi:10.1016/j.msea.2004.08.002.

Krings, A. *et al.* (2017) "Electric Machines," *IEEE Transactions on Industrial Electronics*, 64(3), pp. 2405–2414. doi:10.1109/TIE.2016.2613844.

Kruth, J.P. *et al.* (2004) "Selective laser melting of iron-based powder," in *Journal of*

View publication stats

Materials Processing Technology, pp. 616–622. doi:10.1016/j.jmatprotec.2003.11.051.

Kruth, J.P. *et al.* (2010) "Part and material properties in selective laser melting of metals," in *16th International Symposium on Electromachining, ISEM 2010*.

Letenneur, M., Kreitcberg, A. and Brailovski, V. (2019) "Optimization of laser powder bed fusion processing using a combination of melt pool modeling and design of experiment approaches: Density control," *Journal of Manufacturing and Materials Processing*, 3(1). doi:10.3390/jmmp3010021.

Makoana, N.W. *et al.* (2018) "Characterization of 17-4ph single tracks produced at different parametric conditions towards increased productivity of lpbf systems—the effect of laser power and spot size upscaling," *Metals*, 8(7). doi:10.3390/met8070475.

Matthews, M.J. *et al.* (2016) "Denudation of metal powder layers in laser powder bed fusion processes," *Acta Materialia*, 114. doi:10.1016/j.actamat.2016.05.017.

Muñiz-Lerma, J.A. *et al.* (2018) "A comprehensive approach to powder feedstock characterization for powder bed fusion additive manufacturing: A case study on AlSi7Mg," *Materials*, 11(12). doi:10.3390/ma11122386.

Nickel, A.H., Barnett, D.M. and Prinz, F.B. (2001) "Thermal stresses and deposition patterns in layered manufacturing," *Materials Science and Engineering A*, 317(1–2). doi:10.1016/S0921-5093(01)01179-0.

Palousek, D. *et al.* (2017) "Processing of nearly pure iron using 400W selective laser melting – Initial study," *MM Science Journal*, 2017(FEBRUARY). doi:10.17973/MMSJ.2017_02_2016184.

View publication stats

Parry, L., Ashcroft, I.A. and Wildman, R.D. (2016) “Understanding the effect of laser scan strategy on residual stress in selective laser melting through thermo-mechanical simulation,” *Additive Manufacturing*, 12. doi:10.1016/j.addma.2016.05.014.

“Penn State CIMP-3D” (2020).

“Renishaw - https://www.renishaw.com” (2020).

Rombouts, M. *et al.* (2006) “Fundamentals of selective laser melting of alloyed steel powders,” *CIRP Annals - Manufacturing Technology*, 55(1). doi:10.1016/S0007-8506(07)60395-3.

Simonelli, M. *et al.* (2015) “A Study on the Laser Spatter and the Oxidation Reactions During Selective Laser Melting of 316L Stainless Steel, Al-Si10-Mg, and Ti-6Al-4V,” *Metallurgical and Materials Transactions A: Physical Metallurgy and Materials Science*, 46(9). doi:10.1007/s11661-015-2882-8.

Song, B., Dong, S., Deng, S., *et al.* (2014) “Microstructure and tensile properties of iron parts fabricated by selective laser melting,” *Optics and Laser Technology*, 56, pp. 451–460. doi:10.1016/j.optlastec.2013.09.017.

Song, B., Dong, S., Liu, Q., *et al.* (2014) “Vacuum heat treatment of iron parts produced by selective laser melting: Microstructure, residual stress and tensile behavior,” *Materials and Design*, 54. doi:10.1016/j.matdes.2013.08.085.

Spierings, A.B. *et al.* (2016) “Powder flowability characterisation methodology for powder-bed-based metal additive manufacturing,” *Progress in Additive Manufacturing*, 1(1–2). doi:10.1007/s40964-015-0001-4.

Storn, R. and Price, K. (1997) “Differential Evolution - A Simple and Efficient

View publication stats

Heuristic for Global Optimization over Continuous Spaces," *Journal of Global Optimization*, 11(4). doi:10.1023/A:1008202821328.

Tan, J.H., Wong, W.L.E. and Dalgarno, K.W. (2017) "An overview of powder granulometry on feedstock and part performance in the selective laser melting process," *Additive Manufacturing*, 18, pp. 228–255. doi:10.1016/j.addma.2017.10.011.

Thijs, L. *et al.* (2013) "Fine-structured aluminium products with controllable texture by selective laser melting of pre-alloyed AlSi10Mg powder," *Acta Materialia*, 61(5). doi:10.1016/j.actamat.2012.11.052.

Thomas, M., Baxter, G.J. and Todd, I. (2016) "Normalised model-based processing diagrams for additive layer manufacture of engineering alloys," *Acta Materialia*, 108. doi:10.1016/j.actamat.2016.02.025.

Tiismus, H. *et al.* (2020) "Hysteresis measurements and numerical losses segregation of additively manufactured silicon steel for 3D printing electrical machines," *Applied Sciences (Switzerland)*, 10(18). doi:10.3390/APP10186515.

Tonelli, L. *et al.* (2020) "Effects of powders and process parameters on density and hardness of A357 aluminum alloy fabricated by selective laser melting," *International Journal of Advanced Manufacturing Technology*, 106(1–2), pp. 371–383. doi:10.1007/s00170-019-04641-x.

Vayssette, B. *et al.* (2018) "Surface roughness of Ti-6Al-4V parts obtained by SLM and EBM: Effect on the High Cycle Fatigue life," in *Procedia Engineering*. doi:10.1016/j.proeng.2018.02.010.

View publication stats

Vrancken, B. *et al.* (2014) “Microstructure and mechanical properties of a novel β titanium metallic composite by selective laser melting,” *Acta Materialia*, 68. doi:10.1016/j.actamat.2014.01.018.

Yadav, P. *et al.* (2020) “In situ monitoring systems of the SLM process: On the need to develop machine learning models for data processing,” *Crystals*. doi:10.3390/cryst10060524.

Zhang, M. *et al.* (2016) “Residual stress, defects and grain morphology of ti-6al-4v alloy produced by ultrasonic impact treatment assisted selective laser melting,” *Applied Sciences (Switzerland)*, 6(11). doi:10.3390/app6110304.

View publication stats